

1 **Direct prediction of spatially and temporally varying physical properties**  
2 **from time-lapse electrical resistance data**

3 **Hermans Thomas**, Stanford University, Department of Geological Sciences.

4 **Oware Erasmus**, The State University of New-York at Buffalo, Department of Geology

5 **Caers Jef**, Stanford University, Department of Geological Sciences.

6

7 **Corresponding author**

8 **Hermans Thomas**, Stanford University, Department of Geological Sciences, 450 Serra Mall,  
9 Building 320, Room 118.

10 Phone : 1-650-7232223

11 E-mail : [thermans@stanford.edu](mailto:thermans@stanford.edu)

12 **Running head:**

13 **Direct forecast from TL resistance data**

14

15 **Keypoints:**

- 16 1. We use time-lapse geophysical data to directly forecast physical property in the  
17 subsurface
- 18 2. We use a prior set of models to establish a linear relationship between data and  
19 forecast in a reduced dimension space

20 3. We estimate the full posterior distribution of the physical property with the established  
21 linear relationship for observed data

## 22 **Abstract**

23 Time-lapse applications of electrical methods have grown significantly over the last decade.  
24 However, the quantitative interpretation of tomograms in terms of physical properties, such as  
25 salinity, temperature or saturation, remains difficult. In many applications, geophysical models  
26 are transformed into hydrological models, but this transformation suffers from spatially and  
27 temporally varying resolution resulting from the regularization used by the deterministic  
28 inversion. In this study, we investigate a prediction-focused approach (PFA) to directly estimate  
29 subsurface physical properties with electrical resistance data, circumventing the need for classic  
30 tomographic inversions. First, we generate a prior set of resistance data and physical property  
31 forecast through hydrogeological and geophysical simulations mimicking the field experiment.  
32 We reduce the dimension of both the data and the forecast through principal component analysis  
33 in order to keep the most informative part of both sets in a reduced dimension space. Then, we  
34 apply canonical correlation analysis to explore the relationship between the data and the  
35 forecast in their reduced dimension space. If a linear relationship can be established, the  
36 posterior distribution of the forecast can be directly sampled using a Gaussian process  
37 regression where the field data scores are the conditioning data. In this paper, we demonstrate  
38 PFA for various physical property distributions. We also develop a framework to propagate the  
39 estimated noise level in the reduced dimension space. We validate the results by a Monte Carlo  
40 study on the posterior distribution and demonstrate that PFA yields accurate uncertainty for the  
41 cases studied.

42 **Keywords:** electrical resistance tomography, time-lapse, prediction-focused approach, direct  
43 forecast, inversion

44        **1. Introduction**

45        Over the last few decades, hydrogeophysics has emerged as a new, interdisciplinary, field of  
46        sciences that aims at better understanding of hydrological processes through geophysical  
47        methods. Geophysical surveys are designed to acquire data related to the subsurface such as  
48        subsurface structures (e.g., conceptualization of the aquifer), hydraulic property spatial  
49        distributions (such as porosity and hydraulic conductivity) or the monitoring of physical  
50        properties of an aquifer (e.g., saturation, salinity or concentration, temperature) [e.g., *Rubin and*  
51        *Hubbard, 2005; Vereecken et al., 2007; Binley et al., 2015; Linde et al., 2015*].

52        Among the large number of hydrogeophysical methods (see *Binley et al. [2015]* for a review),  
53        the number of time-lapse applications of electrical methods has grown significantly (see *Singha*  
54        *et al. [2015]* for a review). The electrical resistivity of many fluid bearing sediments and rocks  
55        is largely dominated by the volumetric fluid content and the fluid electrical conductivity. Time-  
56        lapse electrical methods are therefore particularly well-suited for the monitoring of dynamic  
57        processes such as the evolution of saturation in the vadose zone [e.g., *Binley et al., 2002; Koestel*  
58        *et al., 2008*], solute transport [e.g., *Doetsch et al., 2012; Robert et al., 2012*], heat transport  
59        [e.g., *Hermans et al., 2014; Arato et al., 2015*], contaminant remediation operations [e.g., *Truex*  
60        *et al., 2013; Johnson et al., 2015; Masy et al. 2015*] or CO<sub>2</sub> sequestration [e.g., *Carrigan et al.,*  
61        *2013; Auken et al., 2014*]. The goal of hydrogeophysics is not just to quantify the change in  
62        resistivity caused by those processes, but also to infer the related change in physical properties  
63        such as water content and saturation, salinity or temperature. Knowing the spatio-temporal  
64        distribution of such physical properties is important for forecasting/managing purposes in water  
65        resources, agriculture or geothermal applications. Examples include the need to irrigate when  
66        the moisture content is too small, pumping control when salt water intrusion reaches the capture  
67        zone of a well, the adaptation of heat injection or extraction if the temperature reaches a given  
68        threshold in a geothermal system. In addition, regardless of any application, the quantification

69 of the physical properties constitutes a major and fundamental area of research within  
70 hydrogeophysics to study subsurface dynamics [*Singha et al.*, 2015].

71 The most common strategy is to transform geophysical parameters into physical or hydrologic  
72 properties through a petrophysical relationship from field or laboratory measurements [*Singha*  
73 *et al.*, 2015]. The geophysical parameters are most often obtained through a deterministic  
74 regularized inversion. However, the deterministic regularized approach used to invert  
75 geophysical data often yields a smeared distribution of the hydrologic or physical parameters.  
76 Indeed, the solution of the geophysical inverse problem is non-unique and results obtained from  
77 deterministic inversion sometimes lack geological realism [*Linde et al.*, 2015]. Many authors  
78 have observed poor recovery of mass-balance in tracing experiments [e.g., *Singha and Gorelick*,  
79 2005; *Müller et al.*, 2010] and over- or underestimation of the physical properties due to over-  
80 smoothing of the geophysical image [e.g., *Vandenborgh et al.*, 2005; *Hermans et al.*, 2015].  
81 Some authors have proposed alternative constraints to the standard smoothness constraint in  
82 order to reduce smoothing and better estimate physical properties [*Doetsch et al.*, 2010;  
83 *Fiandaca et al.*, 2015; *Caterina et al.*, 2014; *Nguyen et al.*, 2016; *Hermans et al.*, 2016], but the  
84 inherent limitations of deterministic inversion remain.

85 One major issue with the classic deterministic inversion is the spatially varying resolution of  
86 the inversion method that prevents the direct use of petrophysical relationships at the field scale  
87 [*Day-Lewis et al.*, 2005] and strongly depends on the regularization operator. To overcome this  
88 limitation, *Moysey et al.* [2005] and *Singha and Moysey* [2006] proposed Monte Carlo  
89 simulations of numerical analogs of the monitoring experiment to derive a field-scale cell-by-  
90 cell petrophysical relationship, within the modeling grid. Similarly, *Oware et al.* [2013] used  
91 hydrological analog models to derive, through proper orthogonal decomposition (POD), a  
92 physically-based regularization operator able to reproduce physically plausible property  
93 distributions. An underlying limitation of deterministic approaches is their lack of proper

94 uncertainty quantification in the distribution of geophysical parameters, despite that the solution  
95 is known to be non-unique. *Audebert et al.* [2014] developed a method based on multiple  
96 deterministic inversions with various regularization parameters and clustering to better  
97 delineate zone(s) affected by resistivity changes; but their uncertainty concerns only the zone  
98 affected by resistivity changes and not their amplitude.

99 The issue of variable resolution also extends to the time dimension. Time-lapse inversion  
100 schemes with temporal regularization constraints (4D deterministic inversion) have been  
101 developed by *Kim et al.* [2009] and *Karaoulis et al.* [2011]. Even if they generally ensure  
102 coherent variations of geophysical parameters with time, they still suffer from the limitation  
103 arising from regularization.

104 Another approach is the use of summary statistics of the physical property (temporal and spatial  
105 moments) which may be sufficient to identify advection and dispersion effects [e.g., *Kemna et*  
106 *al.*, 2002; *Vandenborghet et al.*, 2005; *Koestel et al.*, 2008]. However, the regularization in the  
107 inversion process still influences the estimation of spatial moments [*Day-Lewis et al.*, 2007].

108 The inverse problem may be formulated in terms of plume geometry [*Ben Hadj Miled and*  
109 *Miller*, 2009; *Pidlisecky et al.*, 2011; *Laloy et al.*, 2012]. In this case, the number of model  
110 parameters is reduced by using the first spatial moments of the geophysical parameter  
111 distribution, making the inverse problem overdetermined and allowing the efficient use of  
112 Markov chain Monte Carlo (MCMC) methods [*Laloy et al.*, 2012]. However, the limited number  
113 of spatial moments used for inversion limits the accuracy of the inverted model in case of  
114 complex geological distributions of the physical properties.

115 The estimated geophysical images or spatial moments, with their inherent limitations, may  
116 subsequently be used, possibly with a petrophysical transformation, to calibrate a  
117 hydrogeological model [e.g., *Binley et al.*, 2002; *Briggs et al.*, 2013]. The modeler may account

118 for the resolution limitations of tomograms by adequately weighting the geophysics-derived  
119 information [*Hermans et al.*, 2012] in order to limit the influence of imperfect estimates of  
120 physical quantities in the calibration process. For example, filtering schemes have been  
121 proposed to account for the varying resolution of tomograms [*Caterina et al.*, 2013] and applied  
122 in hydrogeophysical inversion [*Beaujean et al.*, 2014].

123 An alternative approach is to seek correlation in time between geophysical and hydrological  
124 data. Time series and spectral analysis can provide quantitative information on dynamic  
125 processes occurring in aquifers [*Johnson et al.*, 2012; *Wallin et al.*, 2013]. However, the method  
126 still suffers from the same limitations regarding the inversion itself, such as variable resolution  
127 and lack of (hydro)geological realism.

128 Finally, coupled inversion approaches have gained popularity in the last few years [e.g., *Hinnell*  
129 *et al.*, 2010; *Irving and Singha*, 2010]. In this procedure, geophysical data are directly included  
130 in the hydrologic inversion process, suppressing the need for a geophysical inversion and post-  
131 inversion petrophysical transform. The hydrologic model output is used as input for geophysical  
132 forward modeling through a petrophysical relationship and the corresponding geophysical  
133 response is compared to the observed data. Coupled inversion approaches are efficient when  
134 only a few hydrologic parameters are calibrated but might be difficult to apply in complex and  
135 heterogeneous cases [*Christensen et al.*, 2016], because it strongly depends on the hydrological  
136 conceptual model itself and its inherent assumptions (boundary conditions, prior). The method  
137 also becomes computationally demanding when used within a stochastic framework to quantify  
138 uncertainty [*Irving and Singha*, 2010].

139 In this paper, we propose a prediction-focused approach (PFA) [e.g., *Satija and Caers*, 2015;  
140 *Scheidt et al.*, 2015] to forecast the spatio-temporal change in physical properties using the  
141 changes in resistance collected during time-lapse electrical resistivity tomography (ERT),

142 without explicitly inverting for the resistivity distribution. Note that in this paper we keep the  
143 terminology “forecast” used in previous studies even if the physical property is not estimated  
144 in the future but simultaneously to the data. Similarly to *Moysey et al.* [2005] and *Oware et al.*  
145 [2013], we use analog or prior models to simulate the hydrogeophysical experiment. The use  
146 of aquifer analogs ensures geological realism in the approach, which is essential to produce  
147 physically-plausible results [*Linde et al.*, 2015]. However, instead of using a regularization-  
148 based framework, we aim to directly derive the full posterior distribution of physical properties  
149 from time-lapse ERT, without any iterative inversion. To achieve this, we establish a direct  
150 multivariate statistical model between the data variables (changes in resistance) and the forecast  
151 variables (variations in physical property) in the section where data were collected. We then  
152 use the statistical model to establish a full posterior uncertainty quantification of the forecast  
153 given the actual observed data. Although our method is Bayesian, it differs from previous  
154 Bayesian methods developed in hydrogeophysics and hydrogeology [e.g., *Rubin et al.*, 2010;  
155 *Murakami et al.*, 2010, *Chen et al.*, 2012; *Linde et al.*, 2015]. In PFA, the likelihood is computed  
156 in a reduced dimension statistical framework. Moreover, the likelihood is not formulated based  
157 on the model parameters but based on the target (physical) variables. PFA directly builds a joint  
158 bivariate distribution between data and forecast (target variables) in reduced dimensional space.  
159 From the joint distribution, posterior distribution of forecast given data can then be readily  
160 sampled, without additional forward model evaluations or inversion.

161 *Satiya and Caers* [2015] applied the PFA to forecast the contamination in a pumping well from  
162 concentration measurements upstream from this well, i.e. data and forecast were punctual time  
163 series of the same property. They showed that PFA yields results similar to the rejection  
164 sampler. In this work, we extend the PFA to the use of geophysical data to forecast subsurface  
165 physical properties. We also demonstrate that the method is successful to forecast complex  
166 spatio-temporal series. A topic not covered by *Satiya and Caers* [2015] is the propagation of

167 noise through PFA. This issue is an important concern for geophysical data sets. We propose a  
168 specific framework based on Monte Carlo simulations to prevent erroneous estimates due to  
169 not accounting for the proper noise propagation. With several case examples, we demonstrate  
170 the robustness, methodological and computational simplicity of the approach.

## 171 **2. Methods**

### 172 **2.1. Overview of the methodology**

173 The principle of the PFA is to directly estimate the posterior distribution of the physical  
174 property  $\mathbf{h}$  of interest  $f_H(\mathbf{h}|\mathbf{d}_{obs})$  without explicitly transforming the observed geophysical  
175 data  $\mathbf{d}_{obs}$  into a distribution of geophysical parameters. We therefore avoid inverting the time-  
176 lapse geophysical data sets and using a petrophysical transform *after* inversion that can be  
177 space-dependent and uncertain [Singha *et al.*, 2015]. The key of the PFA is to work in a reduced  
178 dimension space to establish a statistical model between geophysical data and physical  
179 properties to be able to estimate the full posterior distribution of the forecast for some observed  
180 data. The PFA developed for this specific case involves six steps:

- 181 1) generation of prior sets of data and forecast, sampled from the prior distribution,
- 182 2) dimension reduction of the data and forecast variables using principal component analysis,
- 183 3) canonical correlation analysis to establish a multivariate correlation between data and  
184 forecast variables,
- 185 4) Gaussian process regression (kriging) with the observed data to derive the conditional mean  
186 and covariance matrix of the forecast variables (in the canonical component space),
- 187 5) sampling the Gaussian model,
- 188 6) back-transform of the samples into the original high-dimension space.



189 Steps 1 to 3 correspond to the training stage, where the relationship between data and forecast  
190 in the reduced dimension space is learned from forward simulations on the prior set of models.  
191 Steps 4 to 6 correspond to the forecast stage, where the full posterior distribution of the  
192 predictions is deduced from the observed data.

## 193 **2.2. Generating a prior set of models**

194 Establishing a statistical model between data and forecast requires knowing both for some  
195 known subsurface realizations. A realization is the distribution of subsurface parameters  
196 required to simulate data and forecast. We generate a prior set of  $n$  realizations of the  
197 subsurface  $\mathbf{m}$ , here through geostatistical modeling, and simulate (equation 1) the model  
198 response  $\mathbf{h}$  corresponding to the monitored process, here subsurface flow and transport

$$199 \quad \mathbf{h} = g_H(\mathbf{m}) \quad (1)$$

200 where  $g_H$  is the physics-based forward model operator. The model response  $\mathbf{h}$  is generally the  
201 evolution of a given physical property at  $l$  different locations at  $t$  different time-steps in the  
202 subsurface. In the prior set,  $\mathbf{h}$  is therefore a high dimension array of  $n$  realizations of  $l \times t$   
203 variables and constitutes the prior distribution of the forecast.

204 Then, for each realization of this prior, the corresponding geophysical data  $\mathbf{d}$  are computed  
205 using a geophysical forward model  $g_D$

$$206 \quad \mathbf{d} = g_D(\mathbf{h}, \mathbf{m}) \quad (2)$$

207 For ERT, the data are changes in resistance at  $t$  different time steps (subtraction with the  
208 background) for  $u$  different electrode configurations. In the prior set,  $\mathbf{d}$  is therefore an array of  
209  $n$  realizations of  $u \times t$  variables, also high dimensional.

210 Since  $\mathbf{h}$  is a physical property and not a geophysical parameter, a petrophysical relationship  
211 linking both is used in  $g_D$ . In time-lapse studies, the relations between the change of physical  
212 properties and geophysical parameters are relatively well-known and more straightforward  
213 [Linde *et al.*, 2015]. The petrophysical relationship can vary depending on the values of  $\mathbf{m}$ ,  
214 which is therefore a parameter of equation 2. Note that the PFA in general remains valid if data  
215 and forecast are not co-located and not simultaneous (the dimension  $t$  can be different for data  
216 and forecast), i.e. the methodology can be applied to a broader range of problems than time-  
217 lapse geophysical inversion [Satija and Caers, 2015].

### 218 **2.3. Dimension reduction of the data and forecast using principal component analysis**

219 Principal component analysis (PCA) is a multivariate analysis technique that aims at  
220 transforming a set of observed variables into a set of linearly uncorrelated variables, called  
221 principal components [Krzanowski, 2000]. Typically, the first  $k$  components of the PCA  
222 decomposition, with  $k \ll n$ , explain almost all the variance of the data set. By keeping only those  
223  $k$  first dimensions, one thus achieves an efficient dimension reduction. PCA is based on the  
224 eigen-decomposition of a matrix and has been applied on training images by Oware *et al.* [2013]  
225 to derive a physically-based operator for the inversion of ERT data. The method is also at the  
226 basis of truncated singular value decomposition which is widely applied to regularize under-  
227 determined inverse problems as those encountered in hydrogeology [e.g. Tonkin and Doherty,  
228 2005].

229 We first apply independently PCA on both the data and forecast variables to reduce their  
230 dimension to  $p$  and  $q$ , respectively. The reduced data and forecast variables after PCA are  
231 denoted by  $\mathbf{d}^f$  ( $p \times 1$ ) and  $\mathbf{h}^f$  ( $q \times 1$ ).

### 232 **2.4. Linearization using canonical correlation analysis between data and forecast**

233 The relationship between  $\mathbf{d}^f$  and  $\mathbf{h}^f$  is often non-linear, due to the petrophysical relationships  
 234 and underlying partial differential equations. Canonical correlation analysis (CCA) is a  
 235 multivariate analysis method that can be used to transform the relationships between pairs of  
 236 vector variables with  $n$  replicates into a set of independent linearized relationships between  
 237 pairs of scalar [Krzanowski, 2000]. Mathematically, CCA finds the coefficients in  $\mathbf{a}_i$  ( $p \times 1$ )  
 238 and  $\mathbf{b}_i$  ( $q \times 1$ ) with  $i = 1 \dots m$  that maximize the correlation between the linear combinations  
 239  $\mathbf{a}_i^T \mathbf{d}^f$  and  $\mathbf{b}_i^T \mathbf{h}^f$ . The resulting linear combinations are denoted by  $\mathbf{d}_i^c$  and  $\mathbf{h}_i^c$ , and called the  
 240 canonical variates of  $\mathbf{d}^f$  and  $\mathbf{h}^f$ . The coefficient of correlation between their  $n$  scalar values is  
 241 called the canonical correlation. The vectors  $\mathbf{a}_i$  ( $p \times 1$ ) and  $\mathbf{b}_i$  ( $q \times 1$ ) are orthogonal to each  
 242 other. The maximum number of canonical variate pairs  $m$  that can be found is the minimum of  
 243 the ranks of  $\mathbf{d}^f$  and  $\mathbf{h}^f$ . Since  $p$  and  $q$  are generally much smaller than  $n$ ,  $m$  corresponds to the  
 244 minimum of  $p$  and  $q$ . The canonical transformation yields two reduced data variables  $\mathbf{d}^c$  and  
 245  $\mathbf{h}^c$ , such that

$$246 \quad \mathbf{d}^c = \mathbf{d}^f \mathbf{A}^T \quad (3)$$

$$247 \quad \mathbf{h}^c = \mathbf{h}^f \mathbf{B}^T \quad (4)$$

248 with  $\mathbf{A} = [\mathbf{a}_1 \dots \mathbf{a}_m]$  and  $\mathbf{B} = [\mathbf{b}_1 \dots \mathbf{b}_m]$ .

249 The canonical transformation can be found through the eigen-decomposition of the sample  
 250 covariance matrix [Krzanowski, 2000]. If  $p > q$ , i.e. more dimensions are kept in the data, this  
 251 transformation is reversible

$$252 \quad \mathbf{h}^f = \mathbf{B}^{-1} \mathbf{h}^c \mathbf{B}^T, \quad (5)$$

253 This back transformation to the original space is essential for the last step of the process.

## 254 **2.5. Gaussian process regression**

255 We use Bayes' rule in formulating the problem of estimating the posterior distribution of  $\mathbf{h}$  for  
 256 some observed data  $\mathbf{d}_{obs}$

$$257 \quad f_H(\mathbf{h}|\mathbf{d}_{obs}) = kf_H(\mathbf{h})L(\mathbf{h}|\mathbf{d}_{obs}) \quad (6)$$

258 where  $f_H(\mathbf{h})$  is the prior distribution,  $L(\mathbf{h}|\mathbf{d}_{obs})$  is a likelihood function and  $k$  is a  
 259 proportionality constant. PCA and CCA enable reducing a set of high-dimensional variables  
 260  $(\mathbf{d}, \mathbf{h})$  to another set of much reduced dimension variables  $(\mathbf{d}^c, \mathbf{h}^c)$ , linearly related and whose  
 261 axes are orthogonal. By back transformation of  $\mathbf{h}^c$  in the original space (equation 5), the  
 262 forecasting problem (equation 6) is tantamount to forecasting  $\mathbf{h}^c$  from  $\mathbf{d}_{obs}^c$ . Our goal is thus to  
 263 obtain the posterior distribution

$$264 \quad f_H(\mathbf{h}^c|\mathbf{d}_{obs}^c) = kf_H(\mathbf{h}^c)L(\mathbf{h}^c|\mathbf{d}_{obs}^c) \quad (7)$$

265 If the canonical correlation of the first components of those reduced dimension variables is  
 266 large enough, i.e., that a linear relationship between the respective components of  $\mathbf{d}^c$  and  $\mathbf{h}^c$   
 267 exists, then a Gaussian process regression can be used to solve the problem of estimating  $\mathbf{h}^c$   
 268 from  $\mathbf{d}_{obs}^c$  [Tarantola, 2005].

269 The framework described by Tarantola [2005] assumes a multivariate Gaussian prior  
 270 distribution of  $\mathbf{h}^c$ , with the mean  $\bar{\mathbf{h}}^c$  and covariance  $\mathbf{C}_{Hc}$  estimated from the sample  
 271 distribution. If the marginal distributions of  $\mathbf{h}^c$  are not Gaussian, then a histogram transform  
 272 needs to be performed. We now model the relationship between  $\mathbf{d}^c$  and  $\mathbf{h}^c$  through the linear  
 273 forward model operator  $\mathbf{G}$

$$274 \quad \mathbf{d}^c = \mathbf{G}\mathbf{h}^c \quad (8)$$

275 Because the data  $\mathbf{d}_{obs}^c$  may be contaminated with noise, its reduced dimension transform  $\mathbf{d}_{obs}^c$   
 276 has observational error  $\mathbf{C}_c^d$ . We will see in the next section how we can model  $\mathbf{C}_c^d$ . The  
 277 likelihood (in equation 7) is assumed to be multivariate Gaussian

$$278 \quad L(\mathbf{h}^c | \mathbf{d}_{obs}^c) = \exp\left(-\frac{1}{2}(\mathbf{G}\mathbf{h}^c - \mathbf{d}_{obs}^c)^T \mathbf{C}_c^{d^{-1}} (\mathbf{G}\mathbf{h}^c - \mathbf{d}_{obs}^c)\right) \quad (9)$$

279 hence, the posterior distribution is also multivariate Gaussian. The conditional mean and  
 280 covariance have the following analytical expressions:

$$281 \quad \widetilde{\mathbf{h}}_c = \left(\mathbf{G}^T \mathbf{C}_c^{d^{-1}} \mathbf{G} + \mathbf{C}_{Hc}^{-1}\right)^{-1} \left(\mathbf{G}^T \mathbf{C}_c^{d^{-1}} \mathbf{d}_{obs}^c + \mathbf{C}_{Hc}^{-1} \bar{\mathbf{h}}^c\right) \quad (10)$$

$$282 \quad \widetilde{\mathbf{C}}_H^c = \mathbf{G}^T \mathbf{C}_c^{d^{-1}} \mathbf{A} + \mathbf{C}_{Hc}^{-1} \quad (11)$$

283 Similarly to *Hansen et al.* [2014] and *Satija and Caers* [2015], we use a multivariate Gaussian  
 284 error model obtained from the residual error in the linear regression (equation 8) for the prior  
 285 set to account for the non-perfectly linear relationship between  $\mathbf{d}^c$  and  $\mathbf{h}^c$  generally observed  
 286 for complex systems. The solution in (10) and (11) is modified by adding the covariance term  
 287 of the error model  $\mathbf{C}_T$  to the data observational error  $\mathbf{C}_c^d$ , and the mean error  $\bar{\mathbf{e}}$  to  $\mathbf{d}_{obs}^c$ . We refer  
 288 to *Satija and Caers* [2015] for a detailed description of the Gaussian error model.

289 An obvious advantage of the methodology is that a Gaussian distribution is uniquely defined  
 290 by its mean and covariance (equations 10 and 11), and that sampling a Gaussian distribution is  
 291 straightforward. It is therefore simple to generate  $s$  samples  $\{\mathbf{h}_1^c, \mathbf{h}_2^c, \dots, \mathbf{h}_s^c\}$  of the posterior  
 292 distribution  $f_H(\mathbf{h}^c | \mathbf{d}_{obs}^c)$ , each sample being composed of  $q$  components. By back  
 293 transformation of CCA (equation 5), the  $q$  components of  $\mathbf{h}^f$  are retrieved for the  $s$  samples.  
 294 Then, those  $q$  components (first  $q$  principal components) are used to estimate  $s$  samples of the  
 295 original high-dimension physical property  $\mathbf{h}$ , by multiplying the reduced components by the  
 296 inverse matrix of the eigenvectors of the PCA decomposition. Since the vectors are

297 orthonormal, the inverse matrix is equal to its transpose. Those  $s$  samples are then used to  
 298 estimate the statistical properties of the posterior distribution  $f_H(\mathbf{h}|\mathbf{d}_{obs})$ .

## 299 **2.6. Noise correlation in PCA space**

300 Solving equations 10 and 11 requires the definition of the covariance matrix of observational  
 301 error in the canonical space  $\mathbf{C}_c^d$ . The canonical space is related to the principal component space  
 302 through linear relationships (equation 3), and therefore  $\mathbf{C}_c^d$  is linearly related to the error  
 303 covariance in principal component space  $\mathbf{C}_f^d$  through

$$304 \quad \mathbf{C}_c^d = \mathbf{A}\mathbf{C}_f^d\mathbf{A}^T \quad (12)$$

305 The error covariance in the principal component space expresses the error that is made on the  
 306 estimation of the principal component scores due to the noise on the data. If we express the  
 307 observed data  $\mathbf{d}_{obs}$  as a function of the true data  $\mathbf{d}_{true}$  corrupted by some noise perturbation  $\epsilon$

$$308 \quad \mathbf{d}_{obs} = \mathbf{d}_{true} + \epsilon \quad (13)$$

309 the error on the estimation of principal components can be similarly expressed as

$$310 \quad \epsilon^f = \mathbf{d}_{obs}^f - \mathbf{d}_{true}^f \quad (14)$$

311 However, the noise observed in the data cannot be easily transformed in the principal  
 312 component space. Indeed, the different electrode configurations are affected to various degrees  
 313 by the noise, depending on the strength of the measured signal. The variable transformation in  
 314 PCA will also affect differently the principal components which have decreasing variance  
 315 contributions and are affected differently by noise. Hence obtaining some analytical expression  
 316 for  $\mathbf{C}_f^d$  is unfeasible. We here propose to use Monte Carlo experiments to estimate the effect of  
 317 noise in the principal and canonical component space:

- 318 1) we use established methods to estimate an error model  $\epsilon$  (equation 13), such as  
319 reciprocal measurements in electrical methods [LaBrecque *et al.*, 1996; Flores Orozco  
320 *et al.*, 2012];
- 321 2) for the *first* of the  $n$  samples of the prior set, we replace the noise free data set by noisy  
322 data, with a level of noise  $\epsilon$  (equation 13);
- 323 3) we perform PCA on the prior set with the *first* sample contaminated by noise;
- 324 4) we compare the principal components of the *first* sample for noisy and noise free data  
325 set to deduce  $\epsilon_1^f$  (equation 14);
- 326 5) we repeat step 2 to 4 for all other  $n-1$  samples of the prior set;
- 327 6) we use the obtained set of errors in principal component space  $\{\epsilon_1^f \epsilon_2^f \dots \epsilon_n^f\}$  to estimate  
328  $\mathbf{C}_f^d$ ;
- 329 7) we estimate  $\mathbf{C}_c^d$  (equation 12).

330 The estimated covariance matrix in the canonical space can now be used in equations 10 and  
331 11 to solve the Gaussian process regression.

### 332 **3. Applications**

333 In this section, we demonstrate the ability of PFA in a multi-time step example simulating a  
334 heat tracer experiment. We will test the robustness of the method for noisy data and various  
335 distributions of the reference forecast. For all examples, from  $n$  realizations (see equations (1)  
336 and (2)), we choose one as the reference solution and the corresponding data as the actual  
337 observed data  $\mathbf{d}_{obs}$ . We forecast the posterior distribution after which we can compare the  
338 results with the reference solution.

339 A comparison between PFA and POD [Oware *et al.*, 2013] is presented in the supporting  
340 information files (Text S1 and Figure S1).

### 341           **3.1. Multi time-steps thermal tracer experiment**

342   The methodology is applied here for forecasting a heat tracer experiment. The heat tracer  
343   experiment mimics the injection of heated water ( $\Delta T = 40^\circ\text{C}$ ) into a confined alluvial aquifer  
344   for 24 hours at a rate of  $3 \text{ m}^3/\text{h}$ . The tracer flows in the aquifer under forced gradient conditions,  
345   induced by pumping at  $30 \text{ m}^3/\text{h}$  in a well located at 20 m from the injection. At 8 m from the  
346   injection well, centered on the direction linking injection and pumping well, a cross-borehole  
347   ERT panel is considered. The distance between the two boreholes is 4.5 m (Figure 1A). The  
348   boreholes are equipped with 13 electrodes spaced every 50 cm from 0.5 to 6.5 m deep, covering  
349   the alluvial deposits (Figure 1B).

### 350           **3.2. Prior set**

351   The alluvial deposits are represented by two facies representing sand lenses (30%) in a gravel  
352   (70 %) background. The sand lenses are represented by ellipsoids elongated in the direction of  
353   flow with a maximum length of 5 m, a maximum width of 3 m, and a thickness of 2 m. The  
354   SNESIM algorithm [Strebelle, 2002] is used to simulate 500 unconditional realizations of the  
355   aquifer deposits on a  $40 \times 60 \times 14$  grid with dimensions  $1 \text{ m} \times 1 \text{ m} \times 0.5 \text{ m}$ .

356   For each realization, the heat injection and transport are simulated with HydroGeoSphere  
357   [Therrien *et al.*, 2010] using transient, fully-saturated flow. The model was extended 20 m in  
358   each direction to reduce the effect of boundary conditions on the flow. The boundary conditions  
359   are imposed head mimicking a small natural gradient from the injection to the pumping well  
360   and constant temperatures. Flow and transport parameters are considered constant, i.e. the  
361   variability in the prior is only related to spatial variability in the distributions of the facies. Only  
362   the hydraulic conductivity depends on the facies, it is constant and equal to  $10^{-4}$  and  $5 \times 10^{-2}$   
363   m/s for sand and gravel, respectively.



364 The forecasted property  $\mathbf{h}$  is composed of the variations of temperature in the ERT panel at 20  
365 time-steps (every 6 hours during 5 days), simulated by the flow and transport model. We use  
366 the standard relationship between temperature and water electrical conductivity [*Campbell et*  
367 *al.*, 1948] to derive the corresponding change in electrical conductivity.

$$368 \quad \frac{\sigma_T}{\sigma_{25}} = m_f(T - 25) + 1 \quad (15)$$

369 where  $\sigma_T$  is the water electrical conductivity at temperature  $T$  (in °C) and  $m_f$  is the fractional  
370 change of conductivity by °C. We use  $m_f = 0.02 \text{ } ^\circ\text{C}^{-1}$  in accordance with values found in the  
371 literature [e.g., *Hermans et al.*, 2014] and  $\sigma_{25} = 0.04 \text{ S/m}$ . Both can be easily measured on a  
372 water sample. The background resistivity of sand and gravel are respectively 160 and 120  
373 Ohm.m and we used the ratio of Archie's law between two time-steps to link the change in  
374 water and bulk electrical conductivity. This allows expressing the temperature-dependence of  
375 electrical conductivity without defining the formation factor [*Hermans et al.*, 2014].

376 Based on these resistivity distributions, an ERT resistance data set is simulated for each time  
377 step with a combination of AB-MN and AM-BN bipole-bipole configurations [*Zhou and*  
378 *Greenhalgh*, 2000]. The total number of resistance data is 1436. Finally, we compute the change  
379 in resistance by subtracting at each time step the resistance corresponding to the background  
380 resistivity. This constitutes our data set  $\mathbf{d}$ .

### 381 **3.3. Posterior distribution of the temperature change from noise-free data**

382 The choice of the dimensions  $q$  and  $p$  to retain in PCA is driven by the represented variance  
383 [e.g., *Oware and Moysey*, 2014]. The dimension  $q$  kept for the forecast must therefore represent  
384 enough variance to propose realistic samples of the physical property. For low dimension  
385 forecasts such as a time series at a given location, explaining more than 99% of the variance is  
386 feasible [*Satiya and Caers*, 2015]. However, for high dimension forecasts such as those

387 considered here with two spatial dimensions and one temporal dimension, a lower cut-off is  
388 expected.

389 Part of the data may be uninformative about the forecast, hence it is not always necessary to  
390 retain 99% or more of the variance of the data to choose the dimension  $p$ . However, we  
391 generally observe an increase in correlation coefficients in CCA when more dimensions are  
392 kept in the data. To ensure the back transform of CCA,  $p$  has also to be higher than  $q$ . As will  
393 be shown in the next section, the choice of the dimension should rather be dictated by  
394 considerations on the noise level and kept to a level sufficiently low compared to the number  
395 of models in the prior set.

396 The noise free data is composed of 20 series of 1436 resistance changes, i.e., a total of 28720  
397 dimensions for each of the 500 realizations. However, resistance data exhibit a very high level  
398 of redundancy and 90% of the spatiotemporal variance is represented by the first 3 principal  
399 components, 99% by the first 12 components and 99.95% by the first 50 dimensions. In this  
400 example, we keep the first 50 dimensions in the data in a reduced data set  $\mathbf{d}^f$ .

401 The forecast is composed of the value of temperature changes at the 28 x 26 cells (25 cm x 25  
402 cm) of the grid used for forward ERT modeling, giving a total of 14560 dimensions for the 499  
403 different realizations of the prior set (the reference forecast is not considered). 90% of the  
404 variance is explained by the first 8 principal components, 95% by the first 14 and 99% by the  
405 first 35 dimensions. We keep the first 14 dimensions in the reduced forecast  $\mathbf{h}^f$ . This ensures a  
406 reliable spatio-temporal reconstruction of the forecast with a relatively low number of  
407 dimensions.

408 CCA is applied on the reduced data sets in order to maximize the correlation between the  
409 components of the data and forecast variables (Figure 2). In this case, the proposed dimension  
410 reduction is efficient: the correlation coefficient for the four first dimensions, carrying most of

411 the variance, is above 0.99. For higher dimensions, a linear relationship is still observed until  
412 dimension 14, supporting the use of the Gaussian regression.

413 We generate 300 samples of the posterior distribution  $f_H(\mathbf{h}^c | \mathbf{d}_{obs}^c)$  which were subsequently  
414 back transformed to the physical space. Four samples of the distribution are shown with the  
415 reference solution at 4 selected time steps in Figure 3. The samples successfully identify the  
416 temporal behavior of the temperature distribution as well as the location and relative spread of  
417 temperature changes. Most differences between samples are related to the value of the  
418 maximum change in temperature. Almost all samples show an abrupt decrease in temperature  
419 at 6 m depth, as observed in the reference solution.

420 The spatial and temporal characteristics of the posterior distribution are summarized in Figure  
421 4. The spatiotemporal mean of the samples slightly overestimates the maximum change in  
422 temperature but clearly identifies the zone affected by a change in temperature. The standard  
423 deviation shows that most variability is related to the time-step exhibiting maximum change  
424 (i.e.,  $t = 36$  h). The maximum value of the standard deviation is observed at the location of the  
425 abrupt temperature decrease, which shows that it is a region difficult to resolve. Figure 4B  
426 shows the mean temperature in the panel at the different time steps for the prior, the posterior  
427 and the reference distributions. This illustrates that the ERT data is very efficient in reducing  
428 uncertainty on the mean temperature in the panel compared to the prior distribution. The PFA  
429 also clearly identifies the temporal behavior of the tracer, because the maximum change in  
430 temperature is not observed at the same time step for the reference as for most of the models in  
431 the prior set (36 h instead of 30 h).

### 432 **3.4. Posterior distribution of the temperature change from noisy data**

433 We perform Monte Carlo simulations with noisy data to evaluate how the noise is propagated  
434 into the PCA component scores. Figure 5 shows the estimated covariance matrix for 2 different

435 cases. The first case corresponds to a 1% random Gaussian noise added to the changes in  
436 resistance. The error thus increases with the change in resistance

437 If the error on the measured resistance is composed of systematic and random components, the  
438 first component is cancelled out when using data difference, but the random component can be  
439 additive. If the actual resistance between two-time steps does not change, but that the random  
440 component does, the resulting error for a zero change in resistance can be as high as for a larger  
441 change in resistance.

442 The second case therefore considers a level of noise independent of the change in resistance.  
443 The error distribution is symmetric around a zero mean with a 0.034 Ohm standard deviation,  
444 the proportion of large errors decreases exponentially: 50% of the absolute errors are below  
445 0.004 Ohm and 90% below 0.0483 Ohm. The histogram of the error distribution is presented  
446 in the supplementary file (Figure S2). The median absolute change in resistance for the whole  
447 data set is 0.018 Ohm; therefore, the ratio of the median absolute error on the median absolute  
448 resistance change is 22 %. The median of the relative error distribution is 18%. The overall  
449 error level is thus much larger than in the first case

450 An illustration of the corresponding noisy data is given in the supporting information figure S2.  
451 The latter case will be referenced as “Independent noise” in the next sections. It is important to  
452 note that the proposed methodology can accommodate any noise description or any noise model  
453 as it does not rely on any specific assumption concerning the noise distribution. An additional  
454 case, with a 10% random Gaussian noise added to the changes in resistance is presented in the  
455 supplementary file (Figures S3 and S4). The interpretation of this case is relatively similar to  
456 the “Independent noise” below.

457 For the 1% Gaussian noise case (first column of Figure 5), the PCA error covariance matrix  $\mathbf{C}_f^d$   
458 is sparse, with only a few non-zero entries along the diagonal. The low level of noise has little

459 effect on the estimation of PCA scores in the first 50 dimensions. The CCA error covariance  
 460 matrix  $\mathbf{C}_c^d$  is computed through equation 12 and shows values close to 0, smaller than the values  
 461 observed in the error model covariance matrix  $\mathbf{C}_T$  whose entries increase with the dimensions,  
 462 as the correlation decreases. This means that the noise has a negligible effect compared to the  
 463 error made in the linear regression. The 1% Gaussian noise does not influence the posterior  
 464 distribution in this case. For the “Independent noise” (second column of Figure 5), the entries  
 465 of  $\mathbf{C}_f^d$  are significantly larger (note the change in the color scale), meaning that the error made  
 466 on the estimated PCA scores is no longer negligible.  $\mathbf{C}_c^d$  entries are one order of magnitude  
 467 above  $\mathbf{C}_T$ . Note that  $\mathbf{C}_T$  is the same as in the first case (only the color scale is different), as it  
 468 only depends on the error in the regression model and thus on the number of dimensions used  
 469 in CCA. An inappropriate estimation of  $\mathbf{C}_c^d$  may lead to a poor estimation of the posterior. Note  
 470 that the estimated  $\mathbf{C}_f^d$  is almost a diagonal matrix, which is expected since the principal  
 471 components are orthogonal and thus uncorrelated.

472 The analysis of  $\mathbf{C}_f^d$  clearly shows that all components are not affected in the same fashion by  
 473 the noise. In the “Independent noise” case, except for the 4<sup>th</sup> dimension, the ten first components  
 474 are well estimated. The error on the PCA scores is particularly high between dimensions 25 to  
 475 40. One possibility is therefore to reduce the number of dimensions in the data set. For example,  
 476 keeping the 25 first dimensions in the data (3<sup>rd</sup> column in Figure 5) still explains 99.7 % of the  
 477 variance and drastically reduces the values of  $\mathbf{C}_c^d$ . Since less dimensions are used, the linear  
 478 regression is weaker and the components of  $\mathbf{C}_T$  are slightly higher than when 50 dimensions are  
 479 kept, such that  $\mathbf{C}_c^d$  is of the same order of magnitude as  $\mathbf{C}_T$ , but only higher dimensions are  
 480 affected.

481 The effects of the choice of the data dimensions and the estimation of the error covariance  
 482 matrix are illustrated in Figures 6 and 7 with the mean and standard deviation of the spatial

483 temperature change for noisy data sets (“Independent noise”). It appears that ignoring the  
484 covariance matrix for noisy data when 50 dimensions are used (2<sup>nd</sup> column in Figures 6 and 7)  
485 yields results contaminated by strong artifacts. The mean of the posterior distribution misses  
486 the spatial patterns and shows no temporal coherence. Due to noise, the poor estimation of the  
487 CCA scores leads to an unacceptable estimation of the forecast. This stresses the importance of  
488 estimating the noise level, as it is the case for standard tomographic inversion. Using the  
489 appropriate estimation of  $\mathbf{C}_c^d$  (3<sup>rd</sup> column) stabilizes the PFA with a mean solution correctly  
490 estimating the spatial and temporal trends but with a higher standard deviation compared to the  
491 noise free case (1<sup>st</sup> column), as expected.

492 Using only 25 dimensions in the data enables reducing the impact of noise (4<sup>th</sup> and 5<sup>th</sup> columns).  
493 Both solutions with and without estimation of  $\mathbf{C}_c^d$  renders results similar to the noise free case.  
494 Given that less dimensions are used,  $\mathbf{C}_T$  has larger values which tends to increase the standard  
495 deviation of the posterior. Taking into account the error covariance matrix has little effect on  
496 both mean and standard deviations, as the poorly estimated dimensions are not considered in  
497 CCA.

498 The proposed noise propagation procedure identifies clearly the risk for the prediction to be  
499 affected by artifacts related to the noise on the data. By analyzing the error covariance matrix  
500 in PCA scores, the components affected by the noise are easily identified. They can be  
501 disregarded or properly processed by using the covariance matrix for prediction. In this specific  
502 case, the conservative choice is to reduce the dimensions of data variables. Indeed, the noise  
503 introduced when a high number of dimensions is used is counterbalanced by an estimated  
504 covariance matrix with larger components, due to the higher error made on the estimation of  
505 PCA scores. This leads to a higher uncertainty on the temperature estimate.

### 506 **3.5. Applications to high and low temperature references**

507 As shown in Figure 4B, the prior distribution spans a broad range of maximum mean change in  
508 temperature, from 0.5 up to 3.5°C. In the previous application, the reference lies in the middle  
509 of the prior distribution of the forecast, and therefore many realizations in the prior set are  
510 relatively similar to the reference. In this section, we apply the PFA to forecast the temperature  
511 for reference realizations at the extreme ends of the prior distribution of the forecast with  
512 relatively high and low temperature changes respectively. The data correspond to the  
513 “Independent noise” case (see section 3.4) and we use the 25 first PCA components of the data  
514 variables.

515 For a high maximum temperature change (Figures 8 and 10), the zone affected by temperature  
516 changes, its spreading and its maximum amplitude are correctly identified by the samples of  
517 the posterior distributions and the mean. The temporal behavior is also coherent with the  
518 reference solution. We observe somewhat more variations in the posterior distribution (higher  
519 standard deviation) which are related to the higher amplitude of the anomaly.

520 The low temperature change is more difficult to image (Figures 9 and 10). Indeed, low  
521 variations in temperature yield low change in resistance so that the measured signal is low. The  
522 case displayed in Figure 9 has a maximum change in temperature of 1°C. In addition, it shows  
523 a relatively early arrival of the tracer. A change of 1°C corresponds to a change in resistivity of  
524 only about 2%, which is often considered as not interpretable in field-scale time-lapse ERT  
525 [e.g., *Robert et al.*, 2012; *Doetsch et al.*, 2012; *Chretien et al.*, 2014; *Hermans et al.*, 2012,  
526 2015].

527 The two displayed samples identify the early arrival, with a maximum temperature slightly  
528 higher than the reference. Since some samples of the posterior also display lower maximum  
529 temperature changes, the mean solution is relatively close to the reference. The location of the  
530 anomaly is correctly imaged. Given the low temperature change, the uncertainty in the posterior

531 is higher than for the two first examples, showing that many temperature distributions can be  
532 coherent with the data.

533 Figure 10 shows the mean temperature in the panel at the different time steps for the prior, the  
534 posterior and the reference distributions for the cases illustrated in Figures 8 and 9. In both  
535 cases, the reference lies within the posterior distribution whose distributions are much narrower  
536 than the prior. This illustrates that the use of ERT data is very efficient in reducing uncertainty  
537 related to the mean temperature in the panel, even though the “hot“ and “cold“ references are  
538 above the 90% quantile and below the 10% quantile of the prior distribution, respectively. ERT  
539 data also allow the temporal behavior of the tracer to be clearly identified.

540 For the high temperature case, the reference response is between quantiles 10% and 50% of the  
541 posterior. Because many samples are generated between the 10% and 50% quantiles, these two  
542 quantiles are very close. This can be related to the small number of realizations sampled in the  
543 high temperature region of the prior distribution of the forecast by the prior set (the reference  
544 is actually above the 98% quantile of the prior distribution).

545 For the low temperature case, noisy data may produce small decrease in temperature ( $\Delta T < 0$ ),  
546 limited to a few tenth of degrees for some of the samples. This is an indirect effect of the  
547 Gaussian regression where values of  $h_c^d$  are sampled that are not observed in the data. The PFA  
548 is not worse than classical inversions, since similar behaviors are observed in standard  
549 inversions showing positive resistivity changes even if only negative changes are expected. It  
550 highlights the fact that sampling the forecast in the tail of a distribution is challenging and might  
551 require additional models in the prior set.

#### 552 **4. Validation**



553 In this section, we validate the posterior distribution of the forecasted physical properties. *Satiya*  
 554 *and Caers* [2015] and *Scheidt et al.* [2014] validated their direct forecasting methodology in a  
 555 hydrogeological context with rejection sampling. Here, we propose, as an alternative, to  
 556 validate the PFA through a Monte Carlo experiment. In a second step, we verify that the  
 557 sampled posterior distributions are consistent with the geophysical data.

#### 558 **4.1. Monte Carlo experiments**

559 The objective of the Monte Carlo experiments is to show that the posterior distributions  
 560 obtained for many references integrate to the prior distribution. This will show that PFA is an  
 561 appropriate method to sample the posterior distribution.

562 Equation 6 expresses the general form of the posterior distribution given the prior distribution  
 563 and a likelihood function. If we generate Monte Carlo samples to explore the entire data space  
 564 by subsequently using every sample of the prior set as observed data  $\mathbf{d}_{obs}$ , and integrate the  
 565 posterior distributions of the forecast we have:

$$566 \quad \int f_H(\mathbf{h}|\mathbf{d})f_D(\mathbf{d})d\mathbf{d} = \int \frac{L(\mathbf{h}|\mathbf{d})}{f_D(\mathbf{d})} f_H(\mathbf{h})f_D(\mathbf{d})d\mathbf{d} \quad (16)$$

567 where  $f_D(\mathbf{d})$  is the prior distribution of the data. The prior distribution of the forecast is  
 568 independent of  $\mathbf{d}$

$$569 \quad \int f_H(\mathbf{h}|\mathbf{d})f_D(\mathbf{d})d\mathbf{d} = f_H(\mathbf{h}) \int L(\mathbf{h}|\mathbf{d})d\mathbf{d} \quad (17)$$

570 and the integral of the likelihood over the data space is equal to 1 so that we obtain

$$571 \quad \int f_H(\mathbf{h}|\mathbf{d})f_D(\mathbf{d})d\mathbf{d} = f_H(\mathbf{h}) \quad (18)$$

572 Equation 18 states that integrating the  $s$  samples of the posterior for the  $n$  realizations of the  
 573 prior set should give a distribution equal to the prior distribution of the forecast. This offers a  
 574 way to validate that the PFA yields physically plausible samples and to study its validity

575 regarding the number of dimensions kept in the CCA. If equation 18 is not verified, one should  
576 question the number of principal components in the data and forecast used in the CCA.

577 This Monte Carlo validation is illustrated in Figure 11 for 25 and 50 dimensions kept in the  
578 data and 14 in the forecast. The curves correspond to some of the quantiles of the prior and  
579 integrated posterior distribution. In both cases, the integrated posterior distributions are almost  
580 exactly similar to the prior distribution.

#### 581 **4.2.Consistency of the sampled posterior of forecast with data**

582 Our methodology is defined statistically in a reduced dimension space, such that the Gaussian  
583 regression process (or linear inversion) implies that the sampled  $\mathbf{h}^c$  are coherent with the  
584 observed reduced data  $\mathbf{d}_{obs}^c$ . Therefore an objective function (deterministic inversion) or a  
585 likelihood based on the actual observed geophysical data, is not required. There is also no need  
586 for any regularization or to run a forward simulation at any step of the PFA, except to build the  
587 prior set. In fact, the entire procedure can be perfectly parallelized in terms of the forward  
588 modeling.

589 Nevertheless, we verify the consistency of the sampled posterior with the actual geophysical  
590 data [e.g., *Lochbühler et al.*, 2014]. However, since the solution is expressed in terms of  
591 physical property (temperature) and not resistivity and that the data are expressed in terms of  
592 change in resistance, there is no direct way to perform this validation. To overcome this issue,  
593 we use the following workflow:

- 594 1) the resistances of the background data set are deterministically inverted to obtain a  
595 distribution of resistivity  $\rho_{BG}$ , we do not use the true resistivity because they would be  
596 unknown in practice;

597 2) through the petrophysical relationship used for the creation of the prior set (equation  
 598 15), we transform, for each time step, the change in temperature  $\Delta T$  into a change in  
 599 resistivity  $\Delta \rho$  that we add to  $\rho_{BG}$  to get  $\rho_{TL}$ ; note that there is no issue of resolution-  
 600 dependent petrophysical relationship, since no constraint on the model was imposed to  
 601 derive  $\Delta T$ ;

602 3) we compute the resistances for each time step and deduce the data, i.e. the changes in  
 603 resistance  $\Delta R_{calc} = d_{calc}$ ;

604 4) we calculate the data misfit between  $d_{true}$ , the noise free reference data set, and  $d_{calc}$   
 605 through the root-mean-square error (RMS) normalized by the value of RMS between  
 606 noise free and noisy data

$$607 \quad \eta_{RMS} = \frac{\sqrt{\sum_i^{ut} (d_{calc,i} - d_{true,i})^2}}{\sqrt{\sum_i^{ut} (d_{obs,i} - d_{true,i})^2}} \quad (19)$$

608 where  $u$  is the number of resistance data and  $t$  the number of time steps in the monitoring  
 609 process;

610 5) we repeat steps 2 to 4 for the  $s$  samples of the posterior.

611 The above workflow was applied to the samples of the posterior distribution corresponding to  
 612 the 3 reference realizations, i.e., intermediate, high and low mean temperature changes, shown  
 613 respectively in Figures 6, 8 and 9 with 25 dimensions kept in the data and the “Independent  
 614 noise” level. The posterior consists of 300 samples and the histogram of their normalized error  
 615  $\eta_{RMS}$  is shown in Figure 12. For the three cases, the mode of the histogram is around 1, i.e., an  
 616 error corresponding to the noise level in the data. This shows that the proposed methodology is  
 617 able to generate realistic distribution of the physical properties of interest in accordance with  
 618 geophysical data, without explicitly running the geophysical forward operator during the  
 619 inversion process.

## 620        **5. Conclusions**

621        We propose to solve the estimation of physical properties with geophysical data with a direct  
622        forecast approach, the PFA, as an alternative to existing deterministic inversions broadly used  
623        in geophysics. The PFA enables directly estimating the spatio-temporal posterior distribution  
624        of physical properties, such as salinity or temperature, to be directly sampled from geophysical  
625        time-series. The method is based on generating a prior set of models mimicking the experiment  
626        of interest. After dimension reduction of the data and forecast with principal component  
627        analysis and canonical correlation analysis, we use a Gaussian regression in the reduced  
628        dimension space to sample the posterior distribution. Then, the samples in the reduced space  
629        are back transformed to the original space.

630        We applied the PFA in a heat tracer experiment for a broad range of amplitude variations. The  
631        methodology is able to correctly identify the spatio-temporal behavior of the tracer, as well as  
632        the amplitude of the maximum change. The spatio-temporal distribution of temperature is  
633        complex. We retained 14 dimensions explaining 95% of the variance. It signifies that small-  
634        scale features of the forecast corresponding to higher dimensions cannot be reproduced by the  
635        method. The corresponding loss of resolution can be assessed by applying this dimension  
636        reduction on models from the prior set.

637        We proposed to analyze the propagation of noise in the reduced component space through  
638        Monte Carlo simulations to estimate the error covariance matrix in the reduced dimension  
639        space. This step is necessary to stabilize the inversion and shows that reducing the number of  
640        dimension in the data can drastically increase the robustness of the method regarding noise.

641        We validated the approach by verifying the consistency of the samples of the posterior  
642        distribution with the geophysical data and the prior distribution. However, the geophysical  
643        parameters are never explicitly inverted in the PFA.

644 In contrast to hydrogeophysical modeling using standard regularized geophysical inversion  
645 techniques, the method is (i) stochastic, i.e., the solution is composed of samples of the full  
646 posterior distribution and not a single deterministic solution; (ii) it solves the spatio-temporal  
647 physical property distribution and not the geophysical parameter; (iii) it does not require the  
648 definition of a regularization term which is recognized to be the major element preventing  
649 quantitative integration of geophysical data in hydrogeological models. Using physically-based  
650 simulations to build the prior set of model, PFA yields physically plausible forecasts. The key  
651 point is to build a prior set in accordance with the expected response.

652 The major advantage of the methodology is to avoid any regularization procedure required in  
653 deterministic inversions. The solutions therefore do not suffer from any spatial bias, spatially  
654 and temporally varying resolution or uncertainty in the post-inversion petrophysical  
655 transformation. Petrophysics is only required to build the prior set. After this step, there is no  
656 need to run any forward hydrogeological or geophysical simulation. Therefore, the PFA enables  
657 to quickly generate the full posterior distribution of the problem compared to classic stochastic  
658 inversion methods. This remains true for problems with a large number of parameters, as long  
659 as it is possible to efficiently reduce their dimensions.

660 Except for building the prior set, the PFA does not require a flow and transport model to  
661 generate the posterior distribution. It is thus more flexible than coupled inversion schemes and  
662 much faster than stochastic MCMC methods. It is therefore a good alternative when only  
663 monitoring results are needed or to improve sequential inversion scheme with a physically  
664 plausible distribution of the physical property, integrating uncertainty of the estimate.

665 Nevertheless, the method is limited by the choice of prior parameters involved in the  
666 construction of the prior set itself, i.e., on the underlying hydrogeological model and the  
667 petrophysical relationship. Indeed, a satisfactory solution will be found only if the actual data

668 lies in the empirical prior distribution of the prior set. Therefore, the method should not be used  
669 for extrapolation. If the observed data lies outside of the prior distribution, it signifies that the  
670 data is not consistent with the prior. However, this is a limitation for all Bayesian methods,  
671 since the Bayesian model requires for the prior to capture data to avoid prior-data inconsistency.  
672 PFA has the advantage over other techniques to clearly identify such inconsistency using the  
673 joint distribution in the reduced dimension space. Observed data corresponding to extremes of  
674 the data prior distribution might be difficult to forecast. In such a case, it might be necessary to  
675 generate more realizations in the vicinity of the observed data and therefore increase the number  
676 of models in the prior set. Similarly, more models might be needed for prior considering more  
677 uncertain parameters such as geological scenarios, boundary conditions or continuous hydraulic  
678 conductivity distributions. However, the computational cost of the method would remain lower  
679 than stochastic McMC methods.

680 Extending the distribution of prior parameters in the prior set to allow uncertainty on sensitive  
681 parameters such as the petrophysical relationships, the hydraulic conductivity of the deposits  
682 and the heterogeneity would ensure a larger data prior distribution and therefore allow an  
683 application of the prior set to a broader range of observed data. Although physically-based flow  
684 and transport simulations were used to generate the prior set in this study, the PFA applied to  
685 geophysical data could also work with a prior set generated differently (e.g., with a  
686 geostatistical tool). Creating the prior set would be faster but at the expense of geological  
687 realism. The proposed developments will be investigated in future work and tested on a real-  
688 world case study.

## 689 **Acknowledgement**

690 The code and data sets used in this work can be obtained on demand. Please contact the  
691 corresponding author. This work was performed by T. Hermans while being the recipient of a

692 fellowship from the Belgian American Educational Foundation for post-doctoral studies at  
693 Stanford University. We also thank Wallonia-Brussels International and the Vocatio  
694 Foundation for the financial support of T. Hermans during his postdoctoral research stay at  
695 Stanford University. We are grateful to E. Huber and F. Nguyen for their careful readings and  
696 suggestions. We thank the Associate Editor, Andrew Binley, and 4 anonymous reviewers for  
697 their constructive comments.

## 698 **References**

- 699 Arato, A., J. Boaga, C. Comina, M. De Seta, E. Di Sipio, A. Galgaro, N. Giordano, and G.  
700 Mandrone (2015), Geophysical monitoring for shallow geothermal applications - Two  
701 Italian case histories, *First Break*, 33(8), 75–79.
- 702 Audebert, M., R. Clément, N. Touze-Foltz, T. Günther, S. Moreau, and C. Duquennoi (2014),  
703 Time-lapse ERT interpretation methodology for leachate injection monitoring based  
704 on multiple inversions and a clustering strategy (MICS), *Journal of Applied*  
705 *Geophysics*, 111, 320–333, doi:10.1016/j.jappgeo.2014.09.024.
- 706 Auken, E., J. Doetsch, G. Fiandaca, A. V. Christiansen, A. Gazoty, A. G. Cahill, and R.  
707 Jakobsen (2014), Imaging subsurface migration of dissolved CO<sub>2</sub> in a shallow aquifer  
708 using 3-D time-lapse electrical resistivity tomography, *Journal of Applied Geophysics*,  
709 101, 31–41, doi:10.1016/j.jappgeo.2013.11.011.
- 710 Beaujean, J., F. Nguyen, A. Kemna, A. Antonsson, and P. Engesgaard (2014), Calibration of  
711 seawater intrusion models: Inverse parameter estimation using surface electrical  
712 resistivity tomography and borehole data, *Water Resources Research*, 50(8), 6828–  
713 6849, doi:10.1002/2013WR014020.
- 714 Ben Hadj Miled, M. K., and E. L. Miller (2007), A projection-based level-set approach to

715 enhance conductivity anomaly reconstruction in electrical resistance tomography,  
716 *Inverse Problems*, 23(6), 2375–2400, doi:10.1088/0266-5611/23/6/007.

717 Binley, A., P. Winship, L. J. West, M. Pokar, and R. Middleton (2002), Seasonal variation of  
718 moisture content in unsaturated sandstone inferred from borehole radar and resistivity  
719 profiles, *Journal of Hydrology*, 267(3), 160–172.

720 Binley, A., S. S. Hubbard, J. A. Huisman, A. Revil, D. A. Robinson, K. Singha, and L. D.  
721 Slater (2015), The emergence of hydrogeophysics for improved understanding of  
722 subsurface processes over multiple scales, *Water Resources Research*, 51, 3837–3866,  
723 doi:10.1002/2015WR017016.

724 Briggs, M. A., F. D. Day-Lewis, J. B. T. Ong, G. P. Curtis, and J. W. Lane (2013),  
725 Simultaneous estimation of local-scale and flow path-scale dual-domain mass transfer  
726 parameters using geoelectrical monitoring, *Water Resources Research*, 49(9), 5615–  
727 5630, doi:10.1002/wrcr.20397.

728 Campbell, R., C. Bower, and L. Richards (1948), Change of electrical conductivity with  
729 temperature and the relation of osmotic pressure to electrical conductivity and ion  
730 concentration in soil extracts, *Soil Sci. Soc. Am. J.*, 13, 66–69.

731 Carrigan, C. R. et al. (2013), Electrical resistance tomographic monitoring of CO<sub>2</sub> movement  
732 in deep geologic reservoirs, *International Journal of Greenhouse Gas Control*, 18,  
733 401–408, doi:10.1016/j.ijggc.2013.04.016.

734 Caterina, D., J. Beaujean, T. Robert, and F. Nguyen (2013), A comparison study of different  
735 image appraisal tools for electrical resistivity tomography, *Near Surface Geophysics*,  
736 11, 639–657, doi:10.3997/1873-0604.2013022.



737 Caterina, D., T. Hermans, and F. Nguyen (2014), Case studies of incorporation of prior  
738 information in electrical resistivity tomography: comparison of different approaches,  
739 *Near Surface Geophysics*, 12, 451–465, doi:10.3997/1873-0604.2013070.

740 Chen, X., H. Murakami, M. S. Hahn, G. E. Hammond, M. L. Rockhold, J. M. Zachara, and Y.  
741 Rubin (2012), Three-dimensional Bayesian geostatistical aquifer characterization at  
742 the Hanford 300 Area using tracer test data, *Water Resources Research*, 48(6),  
743 W06501, doi:10.1029/2011WR010675.

744 Chrétien, M., J. F. Lataste, R. Fabre, and A. Denis (2014), Electrical resistivity tomography to  
745 understand clay behavior during seasonal water content variations, *Engineering*  
746 *Geology*, 169, 112–123, doi:10.1016/j.enggeo.2013.11.019.

747 Christensen, N.K., S. Christensen, and T.P.A. Ferre (2016), Testing alternative uses of  
748 electromagnetic data to reduce the prediction error of groundwater models, *Hydrology*  
749 *and Earth System Sciences*, 20(5), 1925–1946, doi:10.5194/hess-20-1925-2016.

750 Day-Lewis, F. D., K. Singha, and A. Binley (2005), Applying petrophysical models to radar  
751 travel time and electrical resistivity tomograms: Resolution-dependent limitations,  
752 *Journal of Geophysical Research*, 110, B08206, doi:10.1029/2004JB003569.

753 Day-Lewis, F. D., Y. Chen, and K. Singha (2007), Moment inference from tomograms,  
754 *Geophysical Research Letters*, 34(22), L22404, doi:10.1029/2007GL031621.

755 Doetsch, J., N. Linde, and A. Binley (2010), Structural joint inversion of time-lapse crosshole  
756 ERT and GPR traveltimes data, *Geophysical Research Letters*, 37(24), L24404,  
757 doi:10.1029/2010GL045482.

758 Doetsch, J., N. Linde, T. Vogt, A. Binley, and A. G. Green (2012), Imaging and quantifying

759 salt-tracer transport in a riparian groundwater system by means of 3D ERT  
760 monitoring, *Geophysics*, 77(5), B207–B218, doi:10.1190/geo2012-0046.1.

761 Fiandaca, G., J. Doetsch, G. Vignoli, and E. Auken (2015), Generalized focusing of time-  
762 lapse changes with applications to direct current and time-domain induced polarization  
763 inversions, *Geophysical Journal International*, 203(2), 1101–1112.

764 Flores Orozco, A., A. Kemna, and E. Zimmermann (2012), Data error quantification in  
765 spectral induced polarization imaging, *Geophysics*, 77(3), E227–E237,  
766 doi:10.1190/GEO2010-0194.1.

767 Hansen, T. M., K. S. Cordua, B. H. Jacobsen, and K. Mosegaard (2014), Accounting for  
768 imperfect forward modeling in geophysical inverse problems — Exemplified for  
769 crosshole tomography, *Geophysics*, 79(3), H1–H21, doi:10.1190/geo2013-0215.1.

770 Hermans, T., A. Vandenbohede, L. Lebbe, and F. Nguyen (2012), A shallow geothermal  
771 experiment in a sandy aquifer monitored using electric resistivity tomography,  
772 *Geophysics*, 77(1), B11–B21, doi:10.1190/geo2011-0199.1.

773 Hermans, T., F. Nguyen, T. Robert, and A. Revil (2014), Geophysical Methods for  
774 Monitoring Temperature Changes in Shallow Low Enthalpy Geothermal Systems,  
775 *Energies*, 7(8), 5083–5118, doi:10.3390/en7085083.

776 Hermans, T., S. Wildemeersch, P. Jamin, P. Orban, S. Brouyère, A. Dassargues, and F.  
777 Nguyen (2015), Quantitative temperature monitoring of a heat tracing experiment  
778 using cross-borehole ERT, *Geothermics*, 53, 14–26,  
779 doi:10.1016/j.geothermics.2014.03.013.

780 Hermans, T., A. Kemna, and F. Nguyen (2016), Covariance-constrained difference inversion

781 of time-lapse electrical resistivity tomography data, *Geophysics*, 81(5).

782 Hinnell, A. C., T. P. . Ferré, J. A. Vrugt, J. A. Huisman, S. Moysey, J. Rings, and M. B.  
783 Kowalsky (2010), Improved extraction of hydrologic information from geophysical  
784 data through coupled hydrogeophysical inversion, *Water Resources Research*, 46,  
785 W00D40, doi:10.1029/2008WR007060.

786 Irving, J., and K. Singha (2010), Stochastic inversion of tracer test and electrical geophysical  
787 data to estimate hydraulic conductivities, *Water Resources Research*, 46, W11514,  
788 doi:10.1029/2009WR008340.

789 Johnson, T. C., L. D. Slater, D. Ntarlagiannis, F. D. Day-Lewis, and M. Elwaseif (2012),  
790 Monitoring groundwater-surface water interaction using time-series and time-  
791 frequency analysis of transient three-dimensional electrical resistivity changes, *Water*  
792 *Resources Research*, 48(7), W07506, doi:10.1029/2012WR011893.

793 Johnson, T. C., R. J. Versteeg, F. D. Day-Lewis, W. Major, and J. W. Lane (2015), Time-  
794 Lapse Electrical Geophysical Monitoring of Amendment-Based Biostimulation,  
795 *Groundwater*, 53(6), 920–932, doi:10.1111/gwat.12291.

796 Karaoulis, M., J. H. Kim, and P. Tsourlos (2011), 4D active time constrained resistivity  
797 inversion, *Journal of Applied Geophysics*, 73, 25–34.

798 Kemna, A., B. Kulesa, and H. Vereecken (2002), Imaging and characterisation of subsurface  
799 solute transport using electrical resistivity tomography (ERT) and equivalent transport  
800 models, *Journal of Hydrology*, 267(3-4), 125–146.

801 Kim, J. H., M. J. Yi, S. G. Park, and J. G. Kim (2009), 4-D inversion of DC resistivity  
802 monitoring data acquired over a dynamically changing earth model, *Journal of*

803           *Applied Geophysics*, 68(4), 522–532.

804   Koestel, J., A. Kemna, M. Javaux, A. Binley, and H. Vereecken (2008), Quantitative imaging  
805           of solute transport in an unsaturated and undisturbed soil monolith with 3-D ERT and  
806           TDR, *Water Resources Research*, 44(12), W12411, doi:10.1029/2007WR006755.

807   Krzanowski, W. J. (2000), *Principles of multivariate analysis: A user's perspective*, Oxford  
808           Statistical Series 22, Revised Edition., Oxford University Press, New York.

809   LaBrecque, D. J., M. Miletto, W. Daily, A. Ramirez, and E. Owen (1996), The effects of  
810           noise on Occam's inversion of resistivity tomography data, *Geophysics*, 61(2), 538–  
811           548.

812   Laloy, E., N. Linde, and J. A. Vrugt (2012), Mass conservative three-dimensional water tracer  
813           distribution from Markov chain Monte Carlo inversion of time-lapse ground-  
814           penetrating radar data, *Water Resources Research*, 48(7), W07510,  
815           doi:10.1029/2011WR011238.

816   Linde, N., P. Renard, T. Mukerji, and J. Caers (2015), Geological realism in hydrogeological  
817           and geophysical inverse modeling: A review, *Advances in Water Resources*, 86, 86–  
818           101, doi:10.1016/j.advwatres.2015.09.019.

819   Lochbühler, T., G. Pirot, J. Straubhaar, and N. Linde (2014), Conditioning of Multiple-Point  
820           Statistics Facies Simulations to Tomographic Images, *Mathematical Geosciences*,  
821           46(5), 625–645, doi:10.1007/s11004-013-9484-z.

822   Masy, T., D. Caterina, O. Tromme, B. Lavigne, P. Thonart, S. Hilgsmann, and F. Nguyen  
823           (2016), Electrical resistivity tomography to monitor enhanced biodegradation of  
824           hydrocarbons with *Rhodococcus erythropolis* T902.1 at a pilot scale, *Journal of*

825            *Contaminant Hydrology*, 184, 1–13, doi:10.1016/j.jconhyd.2015.11.001.

826    Moysey, S., K. Singha, and R. Knight (2005), A framework for inferring field-scale rock  
827            physics relationships through numerical simulation, *Geophysical Research Letters*,  
828            32(8), L08304, doi:10.1029/2004GL022152.

829    Müller, K., J. Vanderborght, A. Englert, A. Kemna, J. A. Huisman, J. Rings, and H.  
830            Vereecken (2010), Imaging and characterization of solute transport during two tracer  
831            tests in a shallow aquifer using electrical resistivity tomography and multilevel  
832            groundwater samplers, *Water Resources Research*, 46(3), W03502,  
833            doi:10.1029/2008WR007595.

834    Murakami, H., X. Chen, M. S. Hahn, Y. Liu, M. L. Rockhold, V. R. Vermeul, J. M. Zachara,  
835            and Y. Rubin (2010), Bayesian approach for three-dimensional aquifer  
836            characterization at the Hanford 300 Area, *Hydrology and Earth System Sciences*,  
837            14(10), 1989–2001, doi:10.5194/hess-14-1989-2010.

838    Nguyen, F., A. Kemna, T. Robert, and T. Hermans (2016), Data-driven selection of the  
839            minimum-gradient support parameter in time-lapse focused electric imaging,  
840            *Geophysics*, 81(1), A1–A5, doi:10.1190/GEO2015-0226.1.

841    Oware, E. K., and S. M. J. Moysey (2014), Geophysical evaluation of solute plume spatial  
842            moments using an adaptive POD algorithm for electrical resistivity imaging, *Journal*  
843            *of Hydrology*, 517, 471–480, doi:10.1016/j.jhydrol.2014.05.054.

844    Oware, E. K., S. M. J. Moysey, and T. Khan (2013), Physically based regularization of  
845            hydrogeophysical inverse problems for improved imaging of process-driven systems,  
846            *Water Resources Research*, 49(10), 6238–6247, doi:10.1002/wrcr.20462.

847 Pidlisecky, A., K. Singha, and F. D. Day-Lewis (2011), A distribution-based parametrization  
848 for improved tomographic imaging of solute plumes, *Geophysical Journal*  
849 *International*, 187(1), 214–224, doi:10.1111/j.1365-246X.2011.05131.x.

850 Robert, T., D. Caterina, J. Deceuster, O. Kaufmann, and F. Nguyen (2012), A salt tracer test  
851 monitored with surface ERT to detect preferential flow and transport paths in  
852 fractured/karstified limestones, *Geophysics*, 77, B55–B67.

853 Rubin, Y., and S. Hubbard (2005), *Hydrogeophysics*, Water Science and Technology Library,  
854 Springer, Dordrecht, the Netherlands.

855 Rubin, Y., X. Chen, H. Murakami, and M. Hahn (2010), A Bayesian approach for inverse  
856 modeling, data assimilation, and conditional simulation of spatial random fields,  
857 *Water Resources Research*, 46(10), W10523, doi:10.1029/2009WR008799.

858 Satija, A., and J. Caers (2015), Direct forecasting of subsurface flow response from non-linear  
859 dynamic data by linear least-squares in canonical functional principal component  
860 space, *Advances in Water Resources*, 77, 69–81, doi:10.1016/j.advwatres.2015.01.002.

861 Scheidt, C., P. Renard, and J. Caers (2015), Prediction-Focused Subsurface Modeling:  
862 Investigating the Need for Accuracy in Flow-Based Inverse Modeling, *Mathematical*  
863 *Geosciences*, 47(2), 173–191, doi:10.1007/s11004-014-9521-6.

864 Singha, K., and S. M. Gorelick (2005), Saline tracer visualized with three-dimensional  
865 electrical resistivity tomography: Field-scale spatial moment analysis, *Water*  
866 *Resources Research*, 41(5), W05023, doi:10.1029/2004WR003460.

867 Singha, K., and S. Moysey (2006), Accounting for spatially variable resolution in electrical  
868 resistivity tomography through field-scale rock-physics relations, *Geophysics*, 71(4),

869 A25–A28, doi:10.1190/1.2209753.

870 Singha, K., F. D. Day-Lewis, T. Johnson, and L. Slater (2015), Advances in interpretation of  
871 subsurface processes with time-lapse electrical imagin, *Hydrological Processes*, 29(6),  
872 1549–1576.

873 Strebelle, S. (2002), Conditional Simulation of Complex Geological Structures Using  
874 Multiple-Point Statistics, *Mathematical Geology*, 34(1), 1–21.

875 Tarantola, A. (2005), *Inverse problem theory and methods for model parameter estimation*,  
876 Society for Industrial and Applied Mathematics, Philadelphia, PA.

877 Therrien, R., R. McLaren, E. Sudicky, and S. Panday (2010), *HydroGeoSphere: A three-*  
878 *dimensional numerical model describing fully-integrated subsurface and surface flow*  
879 *and solute transport*, Groundwater Simulation Group, Waterloo, ON, Canada.

880 Tonkin, M. J., and J. Doherty (2005), A hybrid regularized inversion methodology for highly  
881 parameterized environmental models, *Water Resources Research*, 41(10), n/a-n/a,  
882 doi:10.1029/2005WR003995.

883 Truex, M. J., T. C. Johnson, C. E. Strickland, J. E. Peterson, and S. S. Hubbard (2013),  
884 Monitoring Vadose Zone Desiccation with Geophysical Methods, *Vadose Zone*  
885 *Journal*, 12(2), 14, doi:10.2136/vzj2012.0147.

886 Vanderborght, J., A. Kemna, H. Hardelauf, and H. Vereecken (2005), Potential of electrical  
887 resistivity tomography to infer aquifer transport characteristics from tracer studies: A  
888 synthetic case study, *Water Resources Research*, 41, W06013,  
889 doi:10.1029/2004WR003774.

890 Vereecken, H., A. Binley, G. Cassiani, A. Revil, and K. Titov (2007), *Applied*

891            *Hydrogeophysics*, NATO Science Series IV. Earth and Environmental Sciences,  
892            Springer, Doordrecht, the Netherlands.

893    Wallin, E. L., T. C. Johnson, W. J. Greenwood, and J. M. Zachara (2013), Imaging high stage  
894            river-water intrusion into a contaminated aquifer along a major river corridor using 2-  
895            D time-lapse surface electrical resistivity tomography, *Water Resources Research*,  
896            49(3), 1693–1708, doi:10.1002/wrcr.20119.

897    Zhou, B., and S. A. Greenhalgh (2000), Cross-hole resistivity tomography using different  
898            electrode configurations, *Geophysical prospecting*, 48(5), 887–912.

899



900 **FIGURE CAPTIONS**

901 Figure 1. A) Experimental set-up of the heat tracing test. B) Electrode location in the ERT  
902 panel.

903 Figure 2. Canonical correlation analysis of the principal components of the change in resistance  
904 data (50 dimensions) and change in temperature (14 dimensions). A linear relation is clearly  
905 visible with correlation coefficient above 0.9 for the first eleven components. The black lines  
906 show the position of the observed data.

907 Figure 3. Reference model and 4 samples of the posterior at 4 different time steps. The  
908 samples correctly catch the spatial and temporal behavior of the temperature distribution. Most  
909 variations between samples are related to the amplitude of the maximum temperature.

910 Figure 4. A) Reference model, mean and standard deviation of the posterior distribution at  
911 different time steps. The mean solution slightly overestimates the maximum temperature but  
912 the reference solution lies within the posterior. The standard deviation amplitude is higher at  
913 the location and time of the maximum temperature change. B) The posterior distribution of the  
914 mean temperature in the panel is displayed with the prior and reference distribution, showing  
915 that the proposed solution is a very good estimator of the mean temperature in the panel (top).  
916 10, 50 and 90% quantiles of the distribution (bottom).

917 Figure 5. Error covariance matrix in PCA space (top), in CCA space (middle row) and Gaussian  
918 regression error model covariance matrix (bottom) for Monte Carlo simulations with change in  
919 resistance data contaminated by 1% random Gaussian noise (left), “Independent noise“ (middle  
920 column) and “Independent noise“ with only the first 25 dimensions considered.

921 Figure 6. Mean of the posterior distribution at four different time steps for various cases: 50  
922 dimensions in the data and noise free data (col. 1), 50 dimensions in the data, noisy data but

923  $C_c^d = 0$  (col. 2), 50 dimensions in the data, noisy data and  $C_c^d$  estimated with Monte Carlo  
924 simulations (col. 3), 25 dimensions in the data, noisy data but  $C_c^d = 0$  (col. 4), 25 dimensions  
925 in the data, noisy data and  $C_c^d$  estimated with Monte Carlo simulations (col. 5).

926 Figure 7. Standard deviation of the posterior distribution at four different time steps for various  
927 cases: 50 dimensions in the data and noise free data (col. 1), 50 dimensions in the data, noisy  
928 data but  $C_c^d = 0$  (col. 2), 50 dimensions in the data, noisy data and  $C_c^d$  estimated with Monte  
929 Carlo simulations (col. 3.), 25 dimensions in the data, noisy data but  $C_c^d = 0$  (col. 4.), 25  
930 dimensions in the data, noisy data and  $C_c^d$  estimated with Monte Carlo simulations (col. 5).

931 Figure 8. Reference model for a high maximum temperature change (col. 1), 2 samples of the  
932 posterior (col. 2 and 3), mean and standard deviation of the posterior distribution (col. 4 and 5).

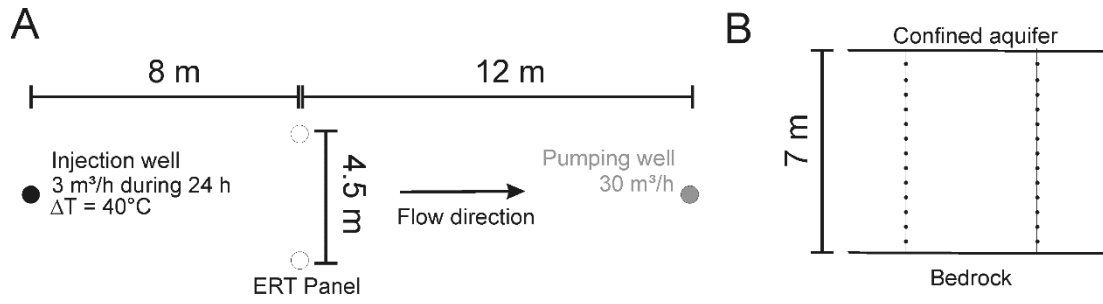
933 Figure 9. Reference model for a low maximum temperature change (col. 1), 2 samples of the  
934 posterior (col. 2 and 3), mean and standard deviation of the posterior distribution (col. 4 and 5).

935 Figure 10. Posterior distribution (10, 50 and 90% quantiles) of the mean temperature in the  
936 panel with the prior and reference distribution for (A) the high and (B) low temperature models.  
937 The bottom row sums up the distributions with the 10, 50 and 90% quantiles for the two cases.

938 Figure 11. The integral of posterior distribution of the temperature in the ERT panel is compared  
939 to the prior distribution using the 10, 25, 50, 75 and 90% quantiles, for (A) 25 dimensions and  
940 (B) 50 dimensions in the data. The distributions are almost exactly similar.

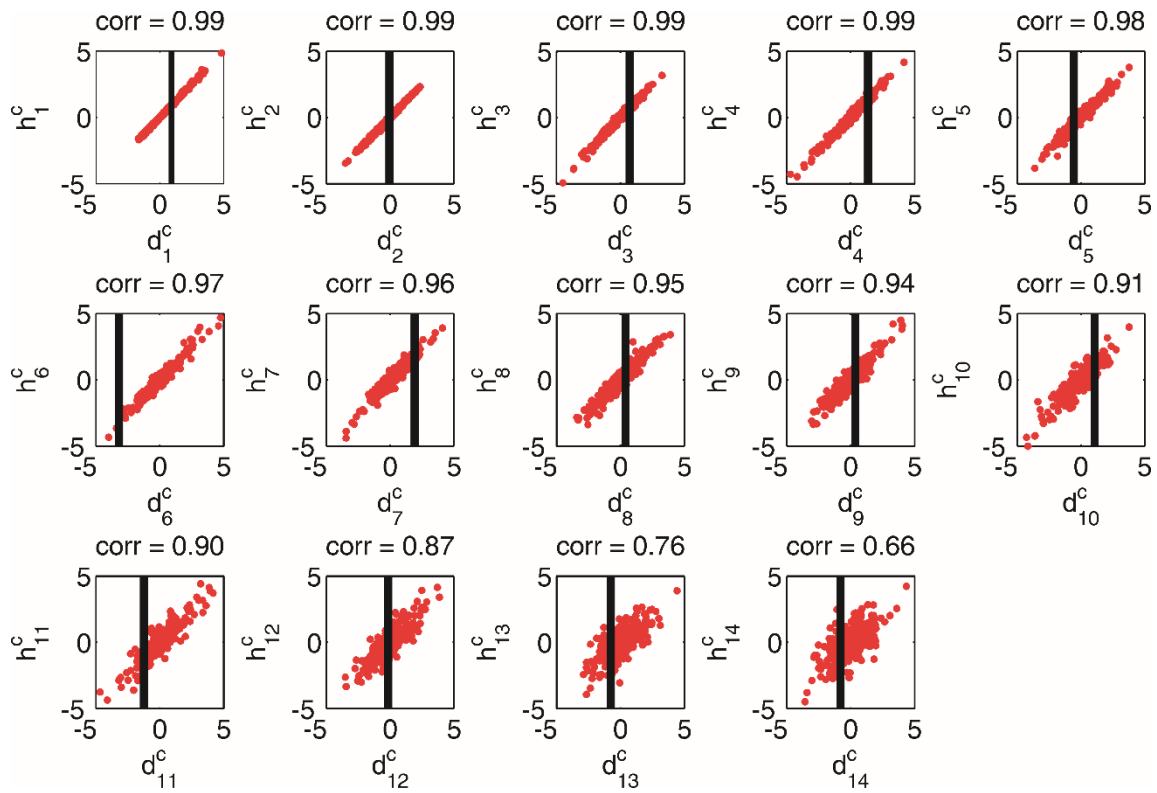
941 Figure 12. Normalized RMS value of the samples of the posterior distribution for (A) the  
942 reference model with intermediate temperature of Figures 6, (B) high temperature of Figure 8  
943 and (C) low temperature of Figure 9. The observed values are within the range of samples fitted  
944 to their noise level in standard inversion.

945



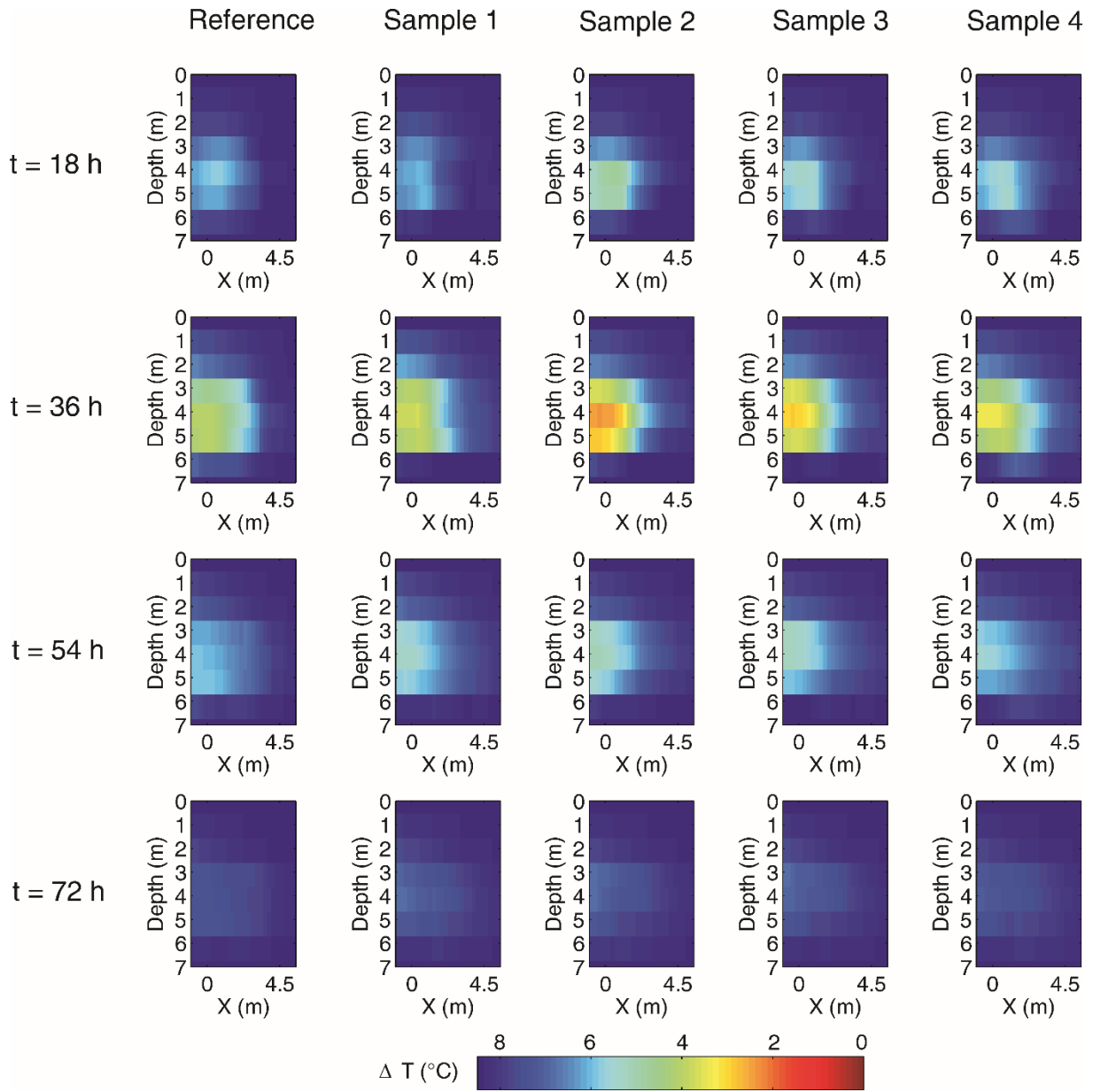
946

947 **Figure 1**



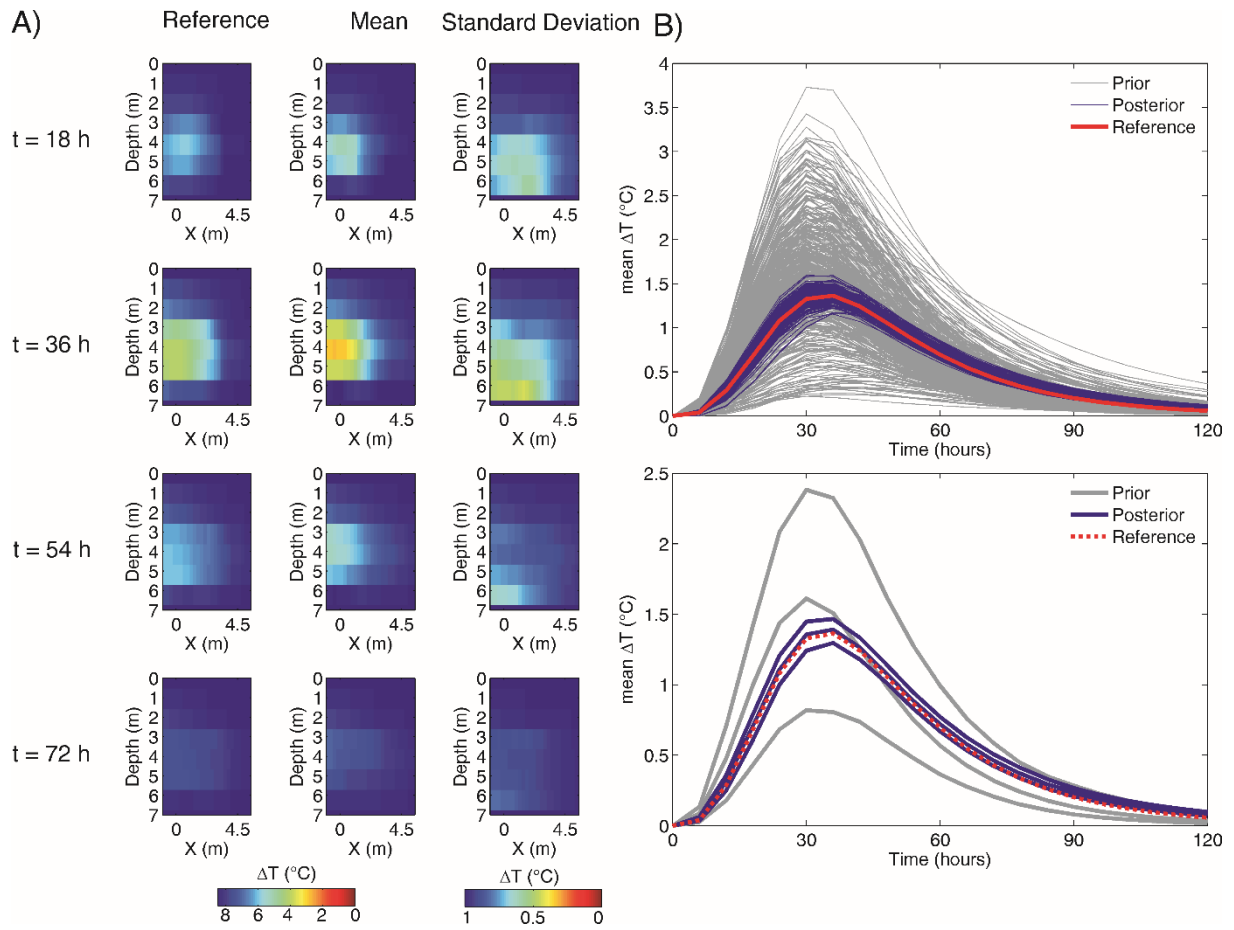
948

949 **Figure 2**



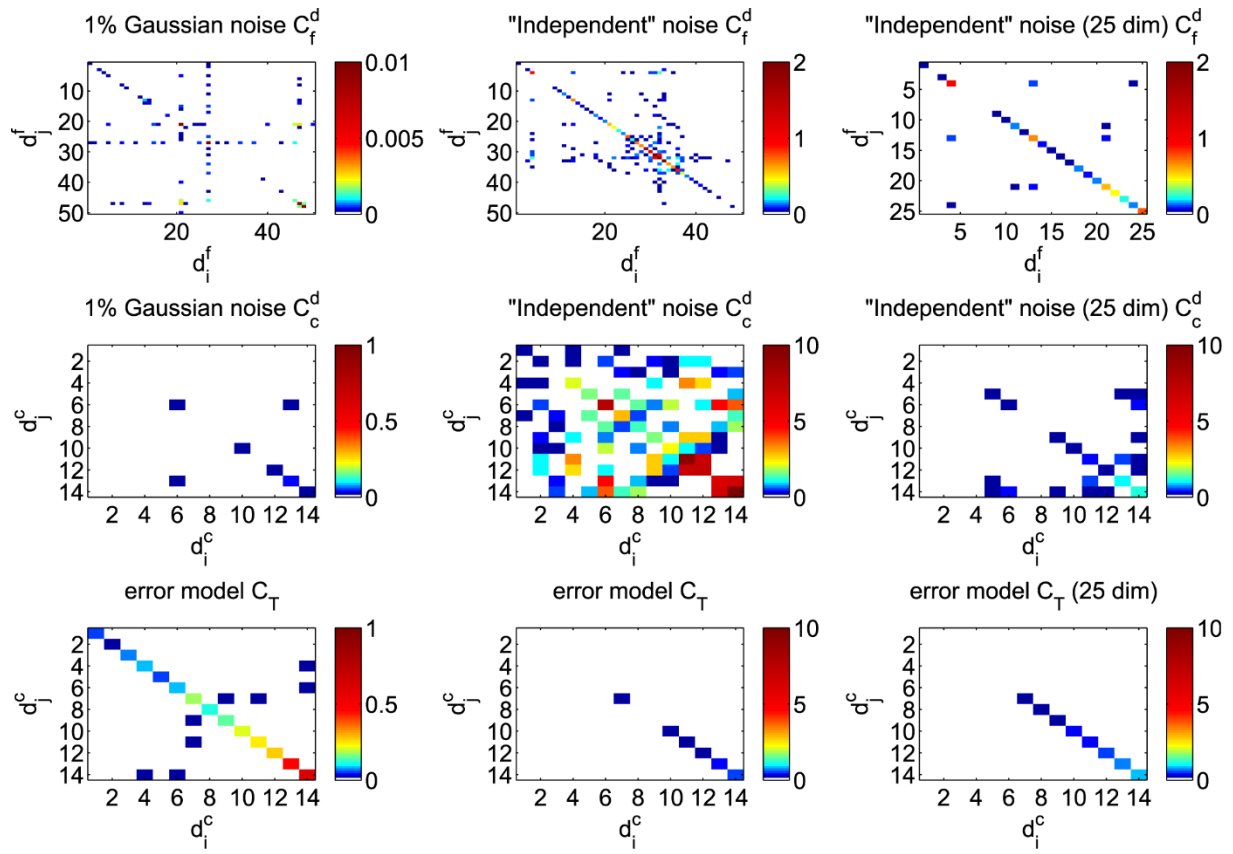
950

951 **Figure 3**



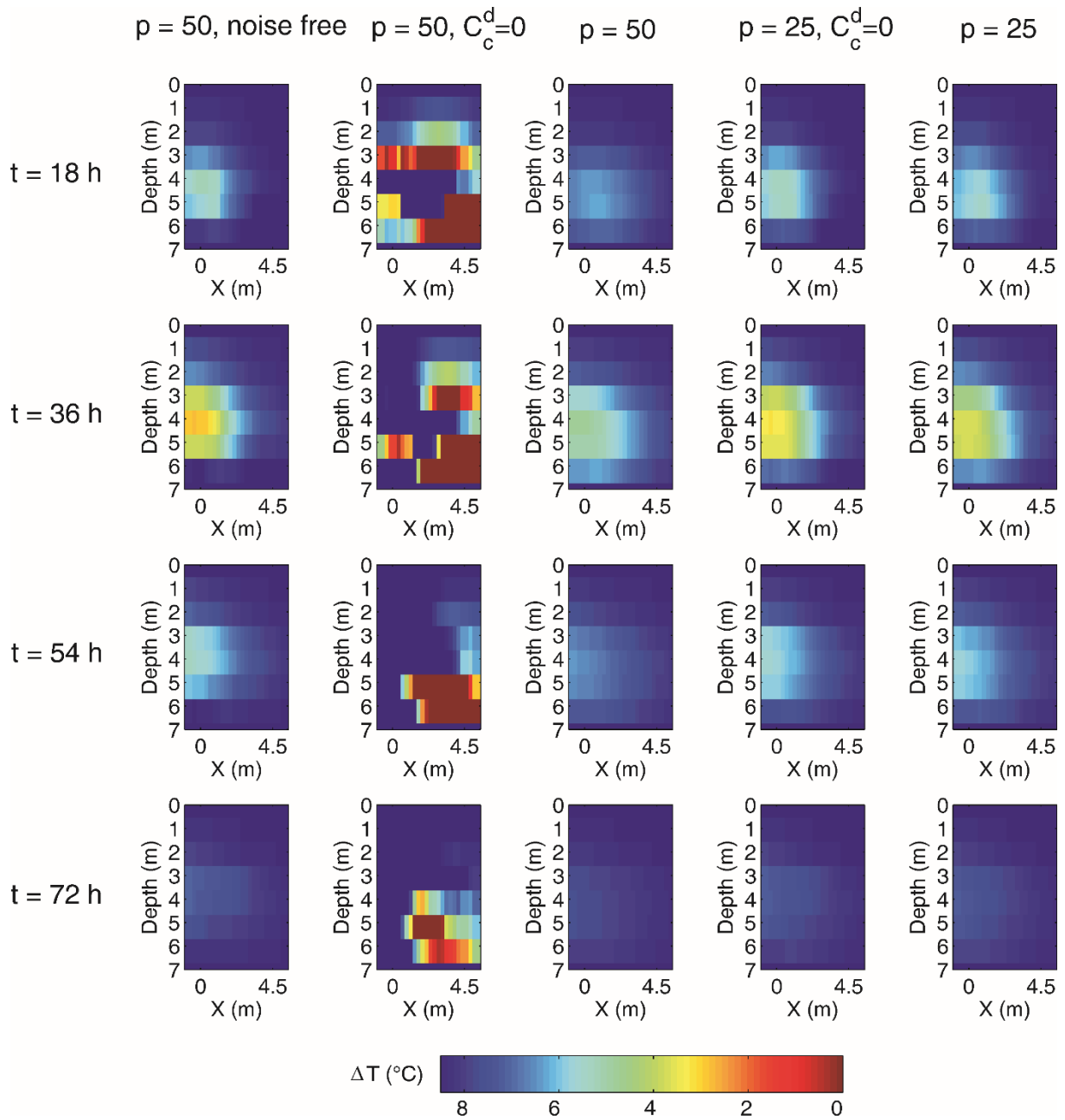
952

953 **Figure 4**



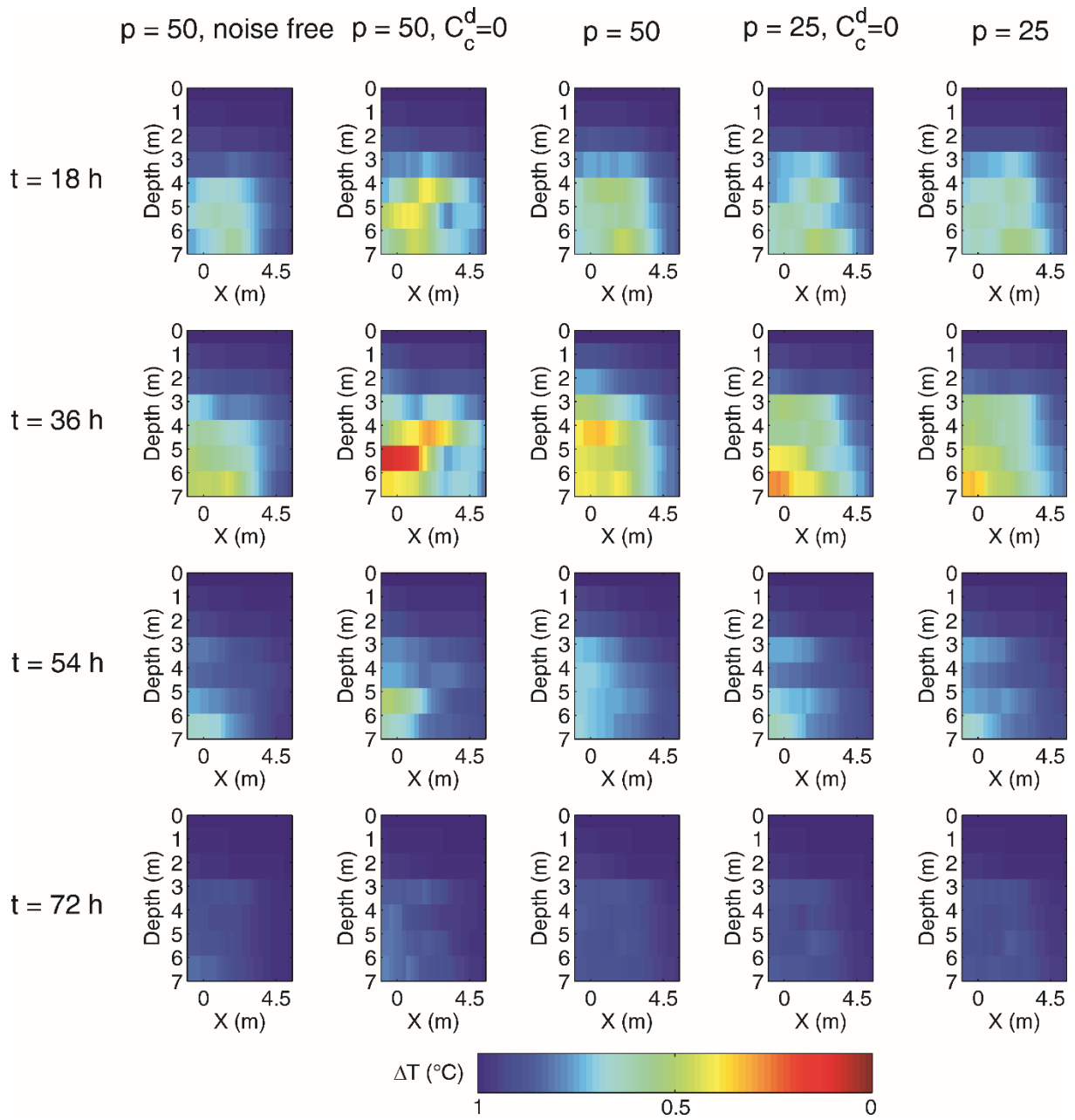
954

955 **Figure 5**



956

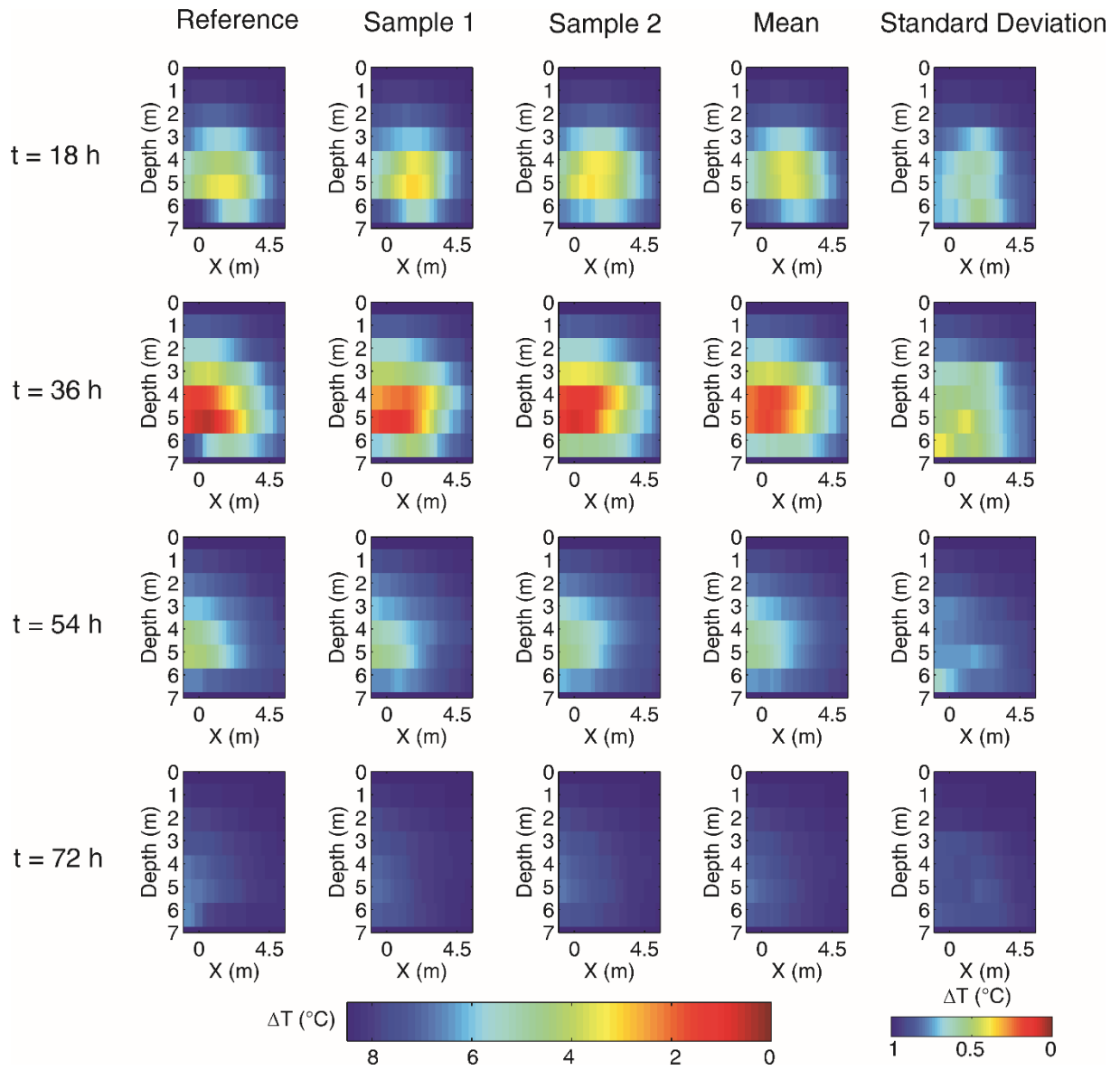
957 **Figure 6**



958

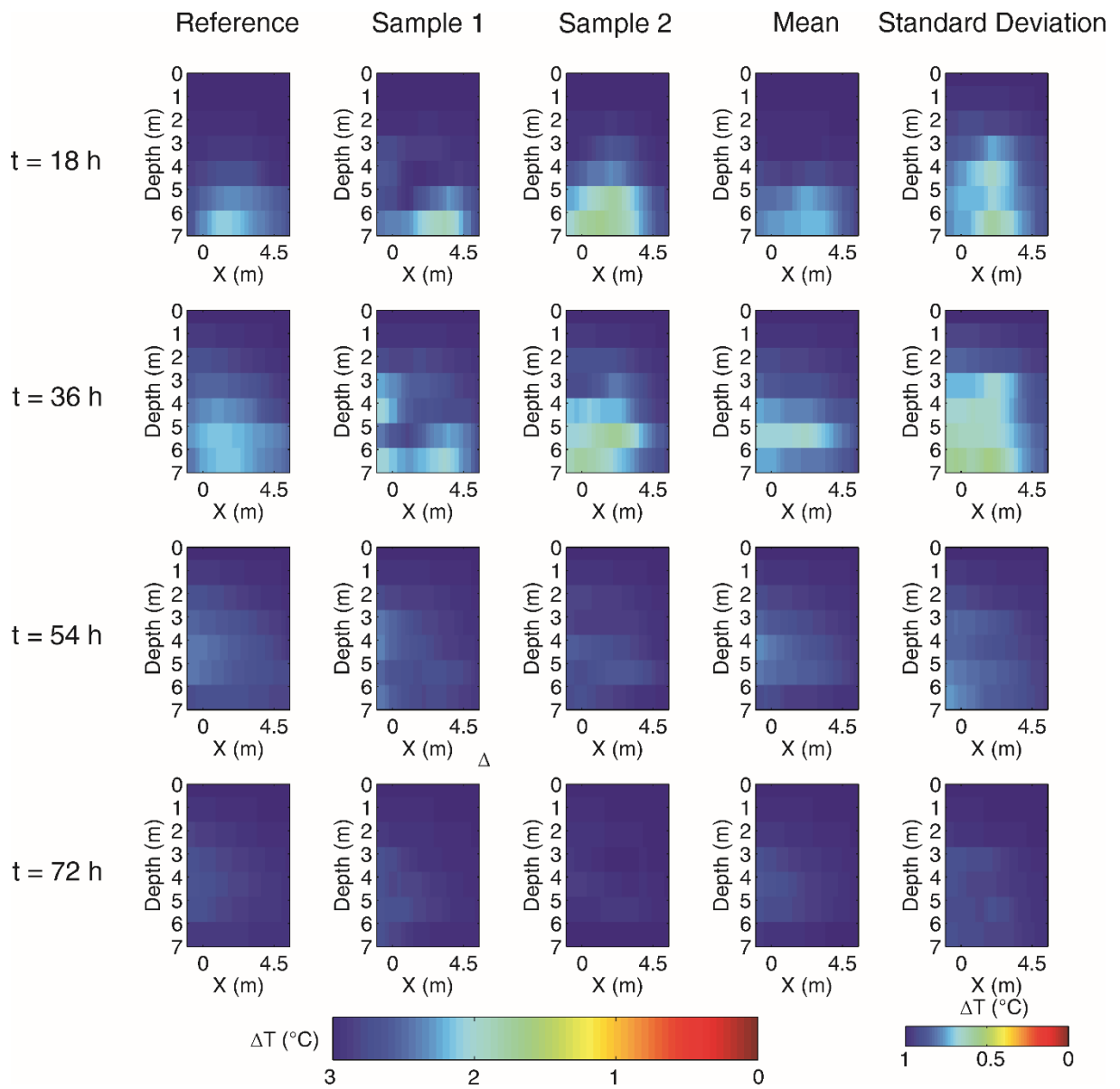
959 **Figure 7**





960

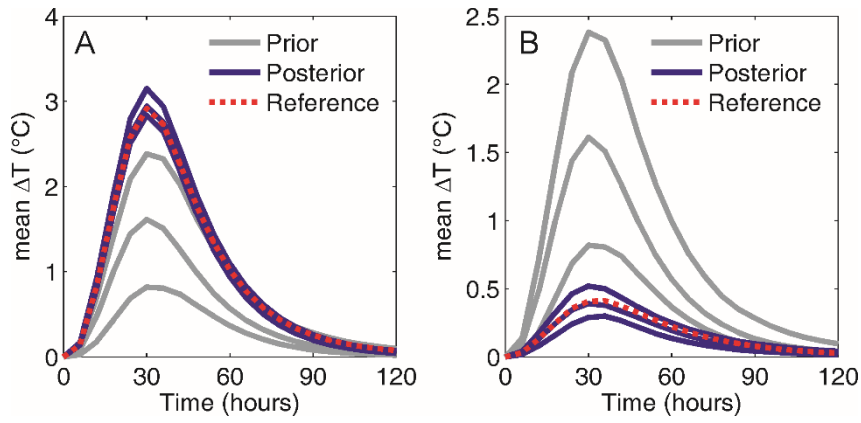
961 **Figure 8**



962

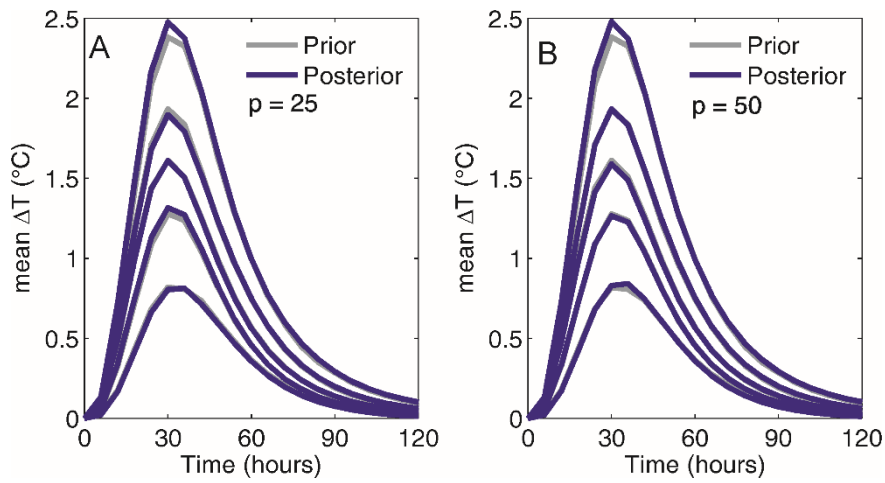
963 **Figure 9**

964



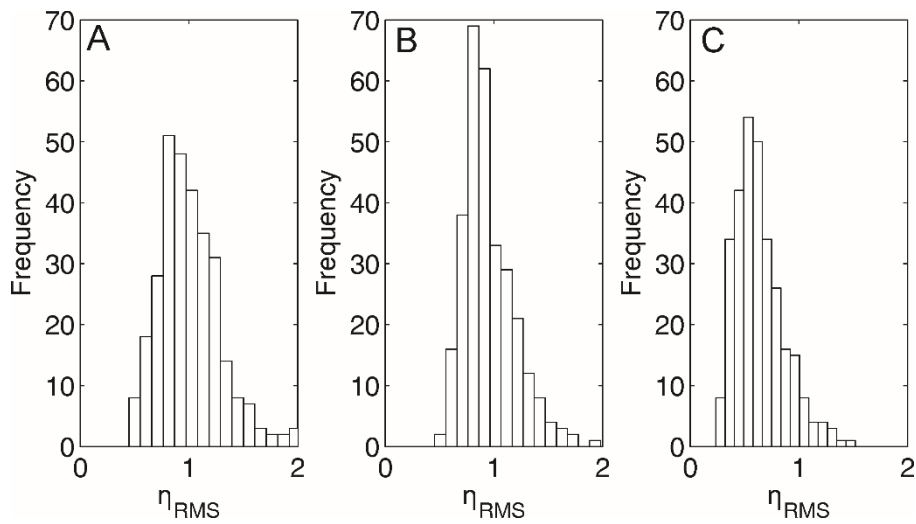
965

966 **Figure 10**



967

968 **Figure 11**



969

970 **Figure 12**